Experimental and Numerical Investigation of Phonon Mean Free Path Distribution
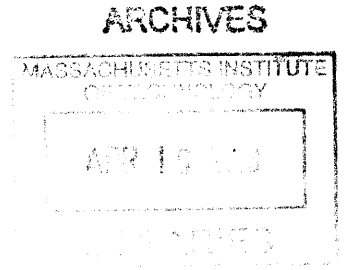
by

Lingping Zeng

Submitted to the Department of Mechanical Engineering
in partial fulfillment of the requirements for the degree of
Master of Science in Mechanical Engineering
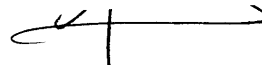
at the

MASSACHUSETTS INSTITUE OF TECHNOLOGY

February 2013

Author...

Department of Mechanical Engineering

February 18, 2013

Certified by ..   ..

Gang Chen

Carl Richard Soderberg Professor of Power Engineering

Thesis Supervisor

Nicolas G. Hadjiconstantinou

Director, Computation for Design and Optimization (CDO)

Co-Advisor

Accepted by ....

David E. Hardt

Chairman, Department Committee on Graduate Students

1

Experimental and Numerical Investigation of Phonon Mean Free Path Distribution

by

Lingping Zeng

Submitted to the Department of Mechanical Engineering
on February 18, 2013, in partial fulfillment of the
requirements for the degree of
Master of Science in Mechanical Engineering

Abstract

Knowledge of phonon mean free path (MFP) distribution is critically important to engineering size effects. Phenomenological models of phonon relaxation times can give us some sense about the mean free path distribution, but they are not accurate. Further improvement of thermoelectric performance requires the phonon MFP to be known. In this thesis, we improve recently developed thermal conductivity spectroscopy technique to experimentally measure MFPs using ultrafast transient thermoreflectance method. By optically heating lithographically patterned metallic nanodot arrays, we are able to probe heat transfer at length scales down to 100 nm, far below the diffraction limit for visible light. We demonstrate the new implementation by measuring MFPs in sapphire at room temperature. A multidimensional transport model based on the grey phonon Boltzmann equation is developed and solved to study the quasi-ballistic transport occurring in the spectroscopy experiments. To account for the nonlinear dispersion relation, we present a variance reduced Monte Carlo scheme to solve the full Boltzmann transport equation and compare the simulation results with experimental data on silicon.

Thesis Supervisor: Gang Chen
Title: Carl Richard Soderberg Professor of Power Engineering

Co-Advisor: Nicolas G. Hadjiconstantinou
Title: Director, Computation for Design and Optimization (CDO)

Acknowledgement

The completion of this thesis would not be possible without the help and support from many individuals. I would like to thank my advisor, Prof. Gang Chen, for offering me the opportunity to work with excellent people and on exciting projects. I benefitted a lot from Gang's advice both on research and on how to communicate effectively with people. Gang's spirit often motivates me to move forward. His patient guidance leads me quickly to learn about the frontier research in the nanoscale heat transfer area and become a more effective researcher. I would like to thank Prof. Nicolas Hadjiconstantinou for serving as my co-advisor and giving me invaluable advice on variance reduced Monte Carlo simulation.

I would like to thank my labmates for giving me much help on how to make the transition from an undergraduate to a graduate student at MIT, on how to handle problems I encountered in my research. Personally, Austin Minnich helped me learn how to solve multi-dimensional phonon Boltzmann Transport equation. Austin Minnich, Kimberlee Chiyoko Collins, Maria Luckyanova frequently helped me to solve pump probe problems in the mean free path experiment. Yongjie Hu, Austin Minnich, Matthew Branham, Anastassios Mavrokefalos gave me helpful advice on how to make the dot array pattern used in pump probe experiment. I am grateful for Keivan Esfarjani's help on phonon theory and simulation. George Ni offered me lots of chance to practice my spoken English and helped me transition smoothly to the life style here at MIT. Thank James and Lei for behaving so nice to me whenever I need help from them. I appreciate whatever kind of help I got from all my labmates at some point. I had a great time with you guys in the last two years.

Prof. Qing Hao at University of Arizona provided much valuable advice on how to simulate phonon transport using traditional Monte Carlo technique. Jean-Philippe Michel Peraud helped me implement the Monte Carlo simulation by solving the energy-based Boltzmann equation.

Most of the sample fabrication was done in Microsystems Technology Laboratory at MIT. I received plenty of help on micro-fabrication from Kurt Broderick. Ebeam Lithography was done at MIT's Scanning Electron Beam Lithography in buildings 38 and Mark Mondol offered great advice on how to make fine features out from Raith. Nabe gave me hands-on experience on how to use the new ebeam machine 'Elionix'. SEM was done in ICL in building 39 and Paul Tierney offered me great help on how to find the pattern easily and get the clearest picture out.

The support of many realized my dream to study at MIT. I would like to give my sincere thankfulness to Prof. Wei Liu, Prof. Suyi Huang, Prof. Tianhua Wu, all at the Huazhong University

.

Contents

9

List of Figures

List of Tables

Chapter 1

Introduction

The ever increasing need for sustainable energy sources has motivated extensive research on different energy technologies. Among them, thermoelectrics [1-3], capable of converting heat directly into electricity without any intermediate process, has made significant progress in terms of the energy conversion efficiency within the last two decades. The increase in efficiency mainly results from significant reductions in the lattice thermal conductivity due to enhanced phonon scattering introduced by either interfaces or boundaries in nanostructured materials, such as nanocomposites, superlattices, and nanowires [4-8]. Such low dimensional materials effectively scatter phonons and lead to dramatic reductions in the lattice thermal conductivity, therefore greatly improving material's performance [9-11]. Further reductions in the thermal conductivity calls for better understanding of the phonon mean free path (MFP) distribution in thermoelectric materials [12-14]. On the other hand, almost all of the established thermal conductivity techniques measure the contributions of integrated effects of all phonons with different MFPs to heat transfer [15-17]. However, a single thermal conductivity value masks the important spectral distribution information of the phonon MFPs, the knowledge of which is critical for engineering size effects in materials to further reduce the lattice thermal conductivity. In this thesis, a thermal conductivity spectroscopy technique [13] combined

with variance reduced Monte Carlo modeling method will be implemented to study phonon MFPs at the nanoscale. This chapter outlines some fundamentals about thermoelectrics, the importance of phonon MFP distribution, and the general idea behind the thermal conductivity spectroscopy technique with nanometer spatial resolution.

1.1 Thermoelectrics

Thermoelectric materials [1] are well known for their capability to convert thermal energy directly into electricity without any intermediate process. The conversion process is based upon the Seebeck effect, observed by Thomas Johann Seebeck in 1821. Seebeck discovered that an applied temperature gradient across the two ends of certain materials generates a voltage difference, which can be used to produce electrical power upon forming a closed circuit. Since thermoelectric devices are solid state and only need a temperature gradient to operate, they have seen applications in spacecraft power generation and waste heat recovery [3].

The efficiency governing the energy conversion in thermoelectric devices is characterized by the dimensionless thermoelectric figure of merit of materials used in the devices defined as $ZT = \frac{S^2 \sigma}{k} T$, where S is the Seebeck coefficient, σ is the electrical conductivity, κ is the thermal conductivity consisting of both the electronic and lattice contributions, and T is the absolute temperature at which the properties are evaluated [18]. The efficiency increases as the ZT increases. Based on the figure of merit, good thermoelectric materials should have high Seebeck coefficient and electrical conductivity, and low thermal conductivity. Succinctly put, candidate materials should behave as 'Phonon-Glass-Electron-Crystal' [19], which refers to the materials with glass-like thermal properties and crystal-like electrical properties. Unfortunately, materials with such desirable properties are not often discovered in nature.

Figure 1-1 shows state-of-the-art ZT through a wide range of temperatures for various materials [12]. Even though the best reported ZT value approaches 1.5, the overall value is

15

still approximately unity. The challenge to improve *ZT* stems from the fact that material properties are strongly inter-correlated [18, 20, 21]. To increase *ZT*, one might try to increase the electrical conductivity of a material. However, this will simultaneously cause the Seebeck coefficient to decrease and the electronic thermal conductivity to increase. These collateral effects are both detrimental to *ZT*. Fortunately, nanotechnology provides possibilities to decouple the transport properties in such a way they can be modified separately.
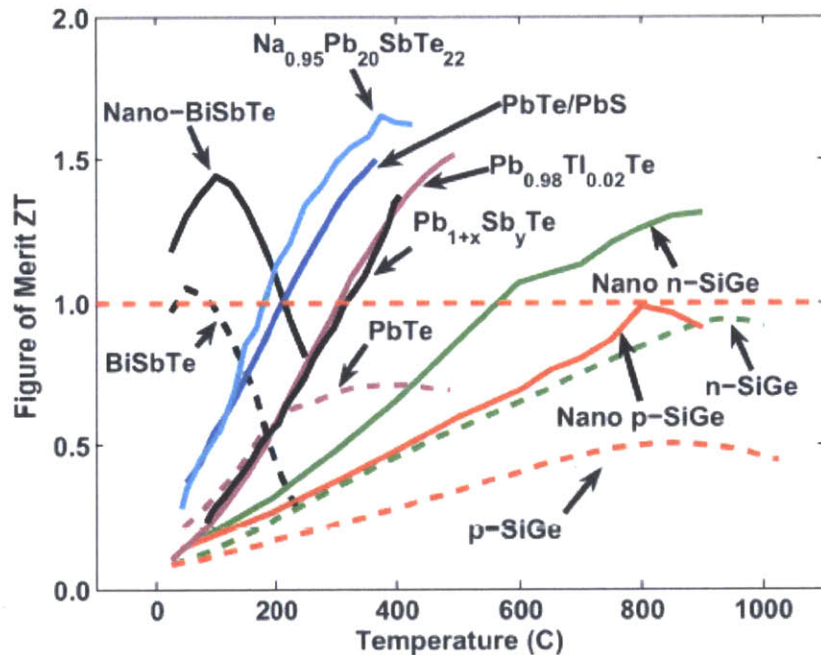
Figure 1-1 State-of-the-art *ZT* values of different materials as a function of temperature [12].

In 1993, Hicks and Dresselhaus [22] proposed a method to selectively modify the material transport properties so that the overall device performance can be improved. They found that low dimensional materials, such as quantum wells and superlattices, can outperform bulk materials and have the potential to enhance *ZT* significantly through electron quantization and enhanced phonon scattering at interfaces. Later, people experimentally demonstrated that nanostructured materials (bulk materials with

incorporation of nanometer scale structures) can significantly increase the thermoelectric efficiency. Poudel *et al.* [4] reported that p-type nanocrystalline BiSbTe alloy can achieve a maximum *ZT* around 1.4 at 100 °C. Hochbaum *et al.* [5] found greatly reduced lattice thermal conductivity of rough silicon nanowires with diameters between 20−300 nm while the Seebeck coefficient and electrical conductivity were almost unaffected. Under room temperature operation Hochbaum achieved *ZT* of ~0.6. Boukai *et al.* [6] compared *ZT* values of silicon nanowires of varying sizes and doping levels with that of bulk silicon over a wide range of temperatures. They demonstrated approximately 100-fold improvement in *ZT* from silicon nanowires compared with their bulk counterpart and attributed the enhancement to the phonon effects introduced by the small nanowires. Venkatasubramanian *et al.* [7] reported significant enhancement in *ZT* from Bi_2Te_3/Sb_2Te_3 thin-film thermoelectric devices by fine-tuning the phonon and electron transport in those devices.

Typically, nanostructured materials have higher densities of grain boundaries and interfaces, which more effectively scatter the heat carriers, i.e. phonons, resulting in a much lower lattice thermal conductivity compared to their bulk counterparts. Phonons are quantized lattice vibrations, which carry certain amount of heat energy while propagating through a material [18, 20, 21]. During their travelling, phonons are subject to various kinds of scatterings, including phonon-boundary scattering, phonon-impurity scattering, and phonon-phonon scattering. The phonon mean free path (MFP) and lifetime describe the average travelling distance and time between two successive scattering events, respectively. The additional scattering introduced by grain boundaries and interfaces in nanostructured materials reduces the effective phonon MFPs and thus their capability to transfer heat [23-25]. Further progress on the nanostructuring approach to improve thermoelectric materials calls for solid understanding of the phonon MFP distribution. However, even though nanostructured materials have a substantially reduced thermal conductivity, the MFP distributions are still unknown. Except for some recent simulation

studies, knowledge of phonon MFP distribution is limited even for most bulk materials and warrants further investigations [13, 26-29]. With known MFP distributions, we can potentially engineer materials to have much lower thermal conductivity and therefore significantly improve thermoelectric materials' performance.

1.2 Importance of Phonon MFPs

As a statistical concept, the phonon MFP measures the average travelling distance between two consecutive phonon scattering events. By definition, the MFP for each phonon mode is the product of the spectral phonon group velocity and lifetime:

$$\Lambda_{\omega,p} = V_{\omega,p}\tau_{\omega,p} \qquad (1\text{-}1)$$

where ω is the angular vibrational frequency, $\Lambda_{\omega,p}$ is the spectral MFP, $V_{\omega,p}$ is the spectral group velocity, $\tau_{\omega,p}$ is the mode dependent lifetime, and p represents different polarizations. Equation (1-1) indicates that MFPs strongly depend upon the phonon modes and scattering details. Contributions of phonons with different MFPs to heat transfer can be examined through the lattice thermal conductivity predicted by the kinetic transport theory [2]:

$$k_{lattice} = \frac{1}{3}\Sigma_p \int_0^{\omega_{max,p}} C_\omega V_{\omega,p}\Lambda_{\omega,p}d\omega \qquad (1\text{-}2)$$

where C_ω is the mode specific heat [18], and $\Lambda_{\omega,p}$ is the spectral phonon MFP. Many semi-empirical phonon lifetime correlations have been developed by matching the model thermal conductivity with experimentally measured data to roughly infer the spectral MFP distribution [30, 31]. However, these empirical correlations do not accurately determine MFPs.

Normally, for a given material, phonon MFP spans several orders of magnitude.

Cumulative thermal conductivity is used to describe the integral contributions of phonons with MFP below a cut-off length scale to heat transfer. The room temperature normalized cumulative thermal conductivity as a function of MFP calculated from first-principles based density functional theory (DFT) is shown in Fig. 1-2 for several different materials [14]. This graph shows the contributions of different phonon MFPs to the total thermal conductivity. For PbTe, approximately 80% contribution to the total thermal conductivity originates from phonons with MFP below 100 nm. For silicon, those phonons only contribute roughly 25% to the total thermal conductivity. Silicon phonon MFP has a very broadly distributed spectrum (varies from several nanometers up to ten micrometers), yet 50% of the total thermal conductivity comes from phonons with MFPs below 500 nm. It is clear that a single averaged MFP number of all phonon modes cannot accurately represent the MFP distribution of a material.
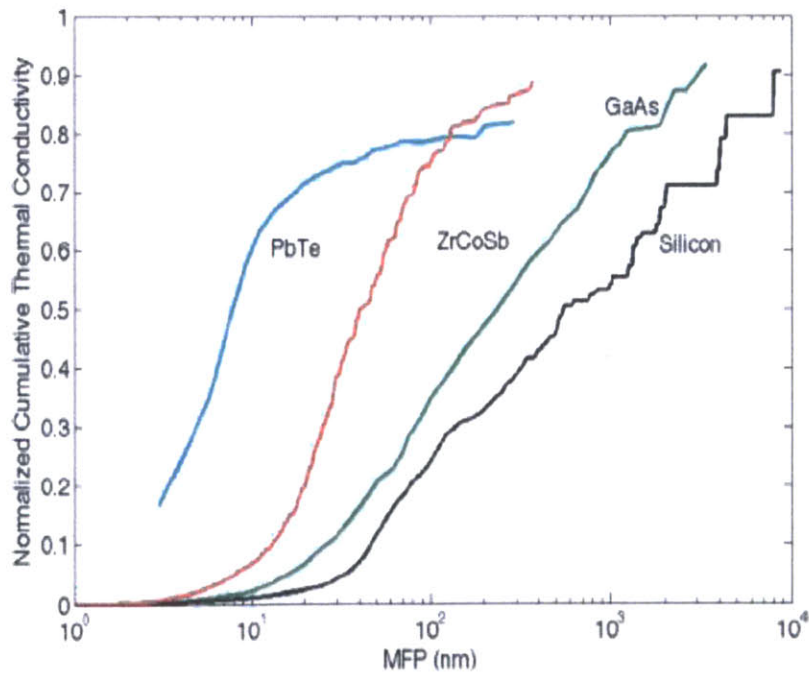
Figure 1-2 Normalized cumulative thermal conductivity vs. MFP [14].

A material's thermal conductivity, as shown in Eq. (1-2), combines the spectral phonon MFP distribution in an integral. When the integral thermal conductivity is measured, all the spectral MFP information is lost. However, engineering size effects requires the MFP knowledge, which helps future efforts into engineering materials that selectively scatter phonons for lower thermal conductivity. Therefore, new strategies must be created to quantify the MFP distribution.

1.3 Thermal Conductivity Spectroscopy

Figure 1-2 indicates that measuring phonon MFPs experimentally requires the study of heat transport at the scales of the heat carriers. In the diffusive transport regime, where the characteristic length scales are much longer than the phonon MFPs, phonons have relaxed to a near local-equilibrium state. Therefore, property measurement in the diffusive regime returns the material's bulk thermal conductivity. However, in the ballistic transport regime, where the characteristic length scales are much shorter than the phonon MFPs, no scattering occurs and phonons have not had a chance to relax to local-equilibrium. Fourier diffusive theory cannot be applied due to the violation of the assumption of massive scattering. Chen [32] showed that the heat flux from a nanoparticle whose dimension is comparable with or smaller than the phonon MFP in the host medium is significantly suppressed compared to the prediction of the Fourier diffusion theory. The reduction of heat flux in the ballistic picture stems from an additional ballistic thermal resistance, whose magnitude depends upon the size of the nanoparticle relative to the phonon MFPs [32, 33]. Since MFPs have a broad spectrum in real materials, the transport becomes quasi-ballistic whenever the length scale falls in the range of MFPs, meaning that some heat carriers with MFPs shorter than the characteristic length (called 'diffusive phonons') travel diffusively while the remaining heat carriers (called 'ballistic phonons') propagate ballistically. Siemens *et al.* [27] confirmed the ballistic resistance in a transient grating

experiment by patterning nanometer scale nickel lines on top of a sapphire substrate and found that the ballistic resistance increases substantially with decreasing contact sizes between the metal nanoline and the sapphire substrate.

An effective thermal conductivity below the bulk value needs to be used in order for Fourier's law to predict correct quasi-ballistic heat transport. The ballistic resistance is inversely correlated with the effective thermal conductivity: the higher the ballistic resistance, the lower the effective thermal conductivity. Since the magnitude of the ballistic resistance depends upon the characteristic length scale relative to the phonon MFPs, so does the effective thermal conductivity. Typically, in quasi-ballistic transport, the shorter the characteristic length scale, the lower the effective thermal conductivity [32]. This indicates that study of quasi-ballistic phonon transport helps extract carrier MFP distribution. Suppose the effective thermal conductivity k_1 is measured at one characteristic length scale L_1. Then we reduce the length scale to L_2 and again measure the effective thermal conductivity k_2. If a big change in the measured effective thermal conductivity is observed, we can conclude that those phonon MFPs within the interval (L_1, L_2) contribute a lot to heat transfer. Otherwise, those phonon MFPs within that length range contribute little to heat transfer. Therefore, measuring the effective thermal conductivities at different length scales in the quasi-ballistic regime yields the contributions of different phonon MFPs to heat transfer in the material being studied.

In practice, quasi-ballistic heat transport can be probed by varying either time scale or length scale. Time domain thermoreflectance (TDTR) [34] and transient thermal grating (TTG) [35] methods are the major tools to map out the spectrum dependent MFPs, mainly at the micrometer scale. In a TDTR experiment Koh and Cahill [26] observed that the thermal conductivity of semiconductor alloys depends strongly on the modulation frequency, which determines the thermal penetration depth and thus affects the transport regime in the alloy sample. They inferred the MFP distribution in those materials by neglecting the contributions of phonons with MFPs longer than the thermal penetration

depth to heat transport. Siemens *et al.* [27] quantified the thermal resistance between lithographically patterned nickel nanolines and a sapphire substrate using ultrafast coherent soft X ray beams. The ballistic thermal resistance in the sapphire substrate was confirmed in the quasi-ballistic regime and found to increase with decreasing contact size when the contact size is below 1 μm. Minnich *et al.* [13] developed a thermal conductivity spectroscopy technique to study phonon MFP distribution for a wide range of length scales using TDTR and demonstrated it through measurements of silicon effective thermal conductivity by systematically varying the heater dimensions (pump laser spot size). It was found that there is a large discrepancy between the measured apparent thermal conductivity and literature bulk thermal conductivity data at low temperatures where phonon MFPs are long. They measured an even lower thermal conductivity with a smaller laser spot size, which again confirmed that ballistic resistance increases with decreasing length scales. In a subsequent TTG experiment Johnson *et al.* [28] reported the deviations of thermal transport in two 400 nm thick freestanding silicon membranes from the prediction of Fourier diffusion theory. The measured effective thermal conductivities on the two Si membranes were significantly lower than the bulk thermal conductivity of Si and also decreased with decreasing the period of the thermal grating due to the transition from diffusive to ballistic transport of low-frequency phonons. These studies opened the way to uncover the mystery of phonon MFPs for many materials.

As discussed before, we desire thermoelectric materials to have low thermal conductivity and therefore short MFPs. For most thermoelectric materials of interest, MFPs are in the range of tens to hundreds of nanometers around room temperature [14]. To probe their MFP distribution, a spectroscopy technique with nanometer spatial resolution is needed. The thermal conductivity spectroscopy technique introduced by Minnich *et al.* cannot be applied directly to probe MFPs at the nanoscale since the highest modulation frequency is around 100 MHz (corresponding to roughly a 500 nm thermal penetration depth for crystalline silicon) and the smallest length scale which can be created

optically is approximately 1 μm for visible light due to diffraction.

To extend the thermal conductivity technique developed by Minnich *et al.* [13] to the nanoscale, the experimental structures were slightly modified [33]. Instead of optically heating a continuous metal film, nanoscale dot arrays are created to act as the heaters. Figure 1-3 shows the nanostructures used in the experiments. A single crystalline sapphire is chosen as the substrate since it is transparent to the laser wavelengths used in our TDTR setup. When pulsed laser beams are applied to heat up the sample, only the metallic dots absorb the laser energy while the substrate is non-absorbing. By illuminating the entire dot array and observing the heat transfer from the dots, the effective length scale becomes the small dot diameter rather than the big laser spot size. Through electron beam lithography (EBL), the heated area size can be systematically varied from tens of microns down to tens of nanometers, thus allowing us to probe much shorter length scales.

| (1a) | (1b) |
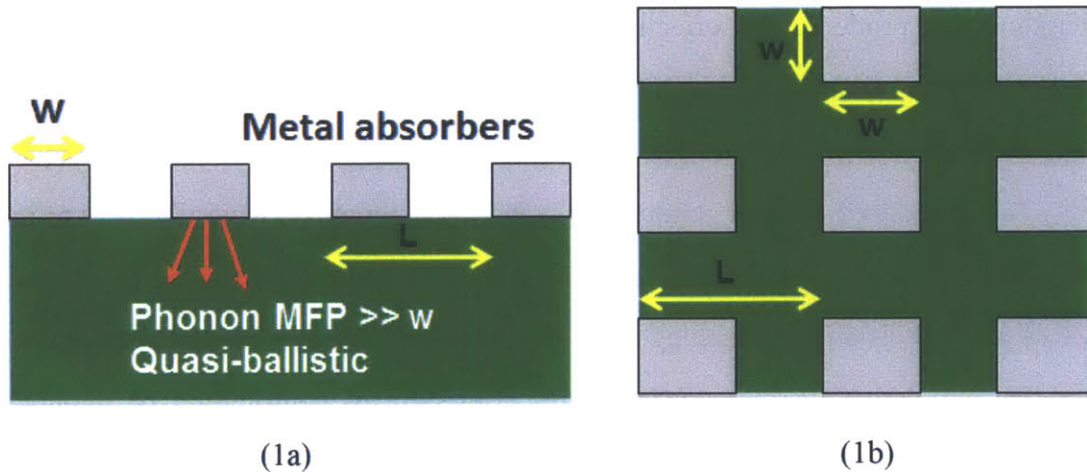
Figure 1-3 Schematic of the nanodots structures used to probe MFPs at the nanoscale: (1a) side view, (1b) top down view. Three important length scales occur in this experiment: the heater size w, the period L, and the phonon MFP in the substrate. When d becomes much smaller than L and the MFP, quasi-ballistic transport in the substrate occurs and heat flow across the interface would be significantly suppressed. When d approaches the period L, transport becomes diffusive due to the presence of sufficient scattering around the interfacial region in the substrate [32, 33].

The periodic heating induced by the pulsed pump beams excites electrons in the

metallic dots, which in turn emit phonons after diffusion through the dots within tens of picoseconds. Subsequently, the excited phonons diffuse through the dots and transmit across the interface between the dots and the substrate, resulting in heat flow through and in the substrate. The scattering probability of the transmitted heat carriers depends upon the heater dimension relative to the phonon MFPs in the substrate [33]. In the limit of large heater size, the transmitted phonons scatter sufficiently and relax to a near equilibrium state, thus diffusive transport occurs and we expect to measure the bulk thermal conductivity of the substrate. When the heater size becomes comparable with a significant fraction of the phonon MFPs, the transmitted phonons with MFPs longer than the heater dimension do not scatter and no local thermodynamic equilibrium can be defined around the interfacial region inside the substrate. In such cases, quasi-ballistic transport dominates the heat transfer process and the presence of an additional ballistic thermal resistance leads to measurement of an effective thermal conductivity lower than the bulk value [32]. Systematically varying the heater dimension across a wide range of length scales produces the effective thermal conductivity distribution, which contains carrier MFP information we need. Minnich *et al.* achieved length scales as low as 400 nm [33]. In this thesis we continue their work to further push the length scale down to 170 nm.

The introduced thermal conductivity spectroscopy method paves the way to measure the phonon MFP distribution with nanometer spatial resolution. However, to determine the MFPs precisely is still challenging since the measured effective thermal conductivities are not the cumulative thermal conductivities consisting of contribution of phonons with MFPs below the heater size. Phonon modes with MFPs above the heater size can also carry a significant amount of heat compared with phonons having short MFPs relative to the heater size, thus contributing to thermal transport. In a recent work, Minnich [36] developed a roadmap to reconstruct the MFPs from the spectroscopy data by solving an integral equation which contains the cumulative MFP distribution function in the integrand. To achieve that, a suppression function which gives the suppression of heat flux for each

phonon mode and is geometry dependent must be known. Minnich demonstrated the technique by inverting the transient grating experimental data on a silicon membrane [28] to obtain the silicon MFPs. A universal suppression function exists for the transient grating geometry [37]. Unfortunately, the suppression function corresponding to each experimental structure in the TDTR thermal conductivity spectroscopy experiments must be found to perform the inversion process to reconstruct the MFPs, which significantly complicates the reconstruction of MFPs in the material being measured.

In addition, we investigate the size dependence of thermal interface conductance [38-40] between aluminum metallic dots and sapphire substrate. Thermal interface conductance is defined as the heat flux across interface divided by the temperature difference on either side of the interface being studied:

$$G = q/\Delta T \tag{1-3}$$

where G is the defined interface conductance, or inverse of interface resistance, q is the heat flux, and ΔT is the temperature difference. The interface conductance characterizes the heat flow rate across the interface of interest. Similar to the substrate thermal conductivity, we simply treat interface conductance as another fitting parameter in the TDTR experiments and study the effect of different length scales on interface conductance in the quasi-ballistic transport regime.

1.4 Organization of this Thesis

This thesis is organized as follows: the first chapter introduced some fundamental concepts

about phonon MFP distribution and its importance to enhancing thermoelectric performance and described the current techniques to measure the MFP distribution. Chapter 2 introduces the developed thermal conductivity spectroscopy technique along with time domain thermoreflectance (TDTR) to measure phonon MFPs and presents the experimentally measured effective thermal conductivity on a sapphire substrate. Chapter 3 develops and solves a multidimensional grey transport model based on the phonon Boltzmann equation for heat transport in structures consisting of periodic nanometer scale metallic lines on top of a generic substrate to study the classical size effects. Chapter 4 describes the use of variance reduced Monte Carlo simulation strategy to investigate the quasi-ballistic transport in the spectroscopy experiments by accounting for the full phonon dispersion relation and spectral lifetimes. Chapter 5 summarizes this thesis and describes the future work.

Chapter 2

Thermal Conductivity Spectroscopy: Probing Phonon MFPs at Nanoscale

2.1 Introduction on Pump-and-Probe Experiments

In chapter one, we emphasized the importance of the phonon MFP distribution in materials of interest for engineering size effects. In this chapter, a thermal conductivity spectroscopy technique combined with the time domain thermoreflectance (TDTR, also called 'pump-and-probe') method [33, 34, 41] is described to investigate phonon MFPs at the nanoscale.

The TDTR technique is a non-contact and non-invasive method which fits well in thermal measurements, especially for layered structures such as thin films and superlattices [41]. Normally the sample consists of two layers: a very thin (~100 nm) optical-thermal transducer metal film sitting on top of the substrate of interest. During the experiment, a periodic laser pulse known as the 'pump' pulse impinges onto the surface of the sample transducer and is partially reflected and partially absorbed. Since electronic heat capacity is very small compared with lattice heat capacity, electrons around the metal film surface are excited to higher energy levels by the pump beam and thus the electronic temperature increases up to several thousand degree Kelvins within hundreds of

femtoseconds [42-45]. The excited electrons quickly thermalize and diffuse through the metal film [46, 47]. The interaction between electrons and phonons transfers the absorbed laser energy from electrons to crystal lattice, raising the lattice temperature. This electron-phonon interaction time is on the order of tens of picoseconds. Excited phonons in the film traverse the metal-substrate interface and interact with phonons in the substrate [48, 49]. Heat transport occurs along with the phonon transmission process.

A second time delayed laser beam known as the 'probe' pulse is used to detect the thermal transport induced by the periodic heating. The time delay is regulated by varying the optical path length of the probe arm through a mechanical stage. The reflectance change at the sample surface is measured versus the delay time between pump and probe beams. A change in the surface reflectance is linearly related to a change in the transducer surface temperature through the thermoreflectance coefficient [50]. Thus, measuring the reflectance change is essentially equivalent to measuring the change in surface temperature history. Lock-in amplification is used to detect the reflected probe signal. The effective thermal properties of interest can be extracted by matching the measured reflectance data to the solution predicted by diffusive heat transfer model. In particular, we are interested in the quasi-ballistic heat transport in the substrate, thus the thermal properties of the substrate [33]. Since Fourier's law is not applicable in the quasi-ballistic regime, an effective substrate thermal conductivity is used when matching the Fourier solution with the measured reflectance data. The distribution of the effective thermal conductivity as a function of different length scales allows us to infer phonon MFP distribution in the substrate being studied. The adoption of effective thermal conductivity is a reasonable approximation, as will be shown by phonon Boltzmann transport equation (BTE) calculations in chapter 3 and variance reduced Monte Carlo models in chapter 4. In this chapter, we introduce the TDTR experimental system and discuss the diffusive thermal model used in the spectroscopy technique to extract the transport properties. Then we proceed to a discussion of the details of sample fabrication. At the end of this chapter,

the measured sapphire thermal conductivity is presented and a summary is given after a discussion of the data.

2.2 TDTR Setup

Researchers have long been taking advantage of optical techniques to perform thermal property measurements. The first pump-and-probe setup was built by Paddock and Eesley in 1986 at the General Motors Research Lab [17]. They used an argon-ion laser to synchronize two ring dye lasers, one with a wavelength of 633 nm and a pulse width of approximately 8ps and the other with a wavelength of 595 nm and a pulse width around 6 ps, which yielded picosecond temporal resolution. In 1996 Capinski and Maris [51] incorporated an optical fiber to direct the probe arm onto the sample. This solved the alignment issue introduced by the mechanical stage used to time delay the probe beam relative to the pump arm. In this way they effectively fixed the probe beam size and position on the sample surface regardless of the probe arm's variable path length. Capinski and Maris also enhanced the experimental time resolution by splitting one laser beam into both the pump and the probe arms. Cahill and coworkers [49] then greatly improved the technique in terms of increasing the signal to noise ratio (SNR) through an introduction of an inductive resonator between the photodetector and lock-in amplifier. The resonator only allows the signal at the resonator frequency to pass and be amplified since the pump beam was also modulated at that frequency. They also made the choosing of measurement spots and focus easier by introducing a CCD camera to visualize the sample on the micrometer stage.

The pump-and-probe setup in the Rohsenow Kendall Heat Transfer Laboratory in the Mechanical Engineering Department at MIT was constructed by a previous PhD student, Dr. Aaron Schmidt, now a professor at Boston University. Our system borrows most of the features of the setup in Professor Cahill's group at University of Illinois at

Urbana-Champaign (UIUC). A very brief description about the setup is given below since others have done that extensively [33, 52-54].
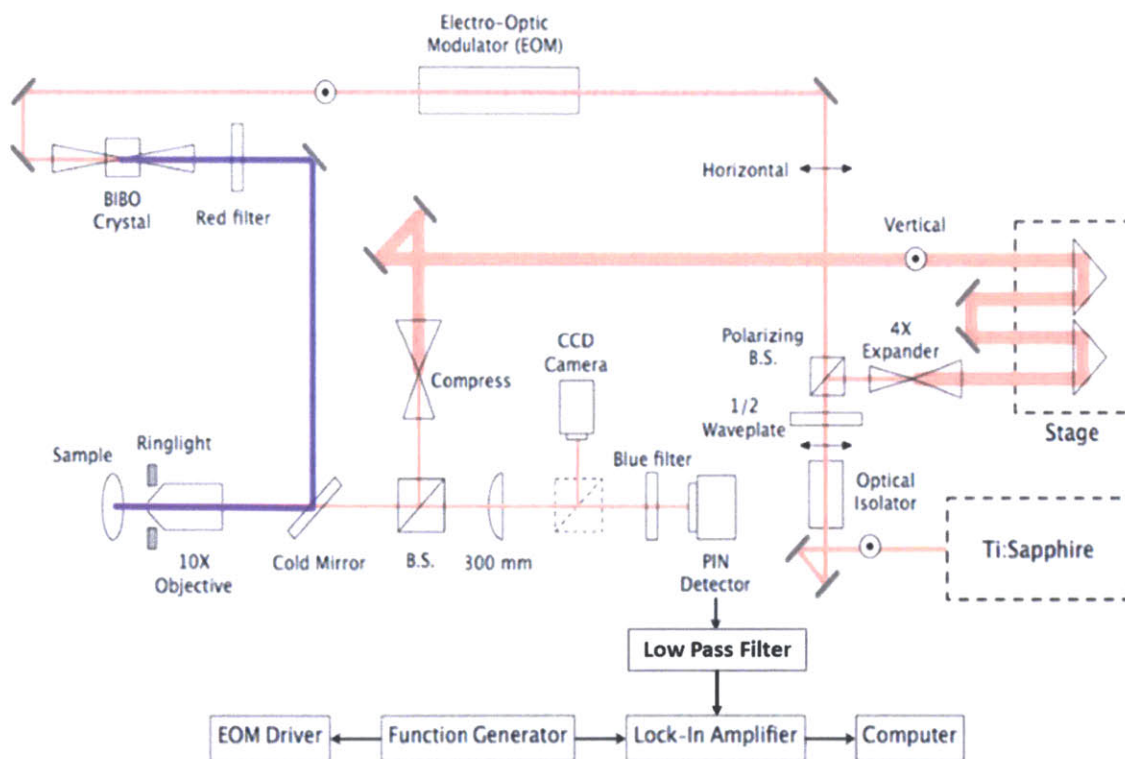
Fig. 2-1 Schematic diagram of the pump-and-probe setup constructed by Dr. Aaron Schmidt. Figure adapted from [52].

A schematic of our experimental setup is shown in Fig. 2-1. The mode locked Ti:Sapphire laser outputs pulses with a wavelength centered around 800 nm and a pulse width of approximately 150 fs at an 80 MHz repetition rate. Such a short pulse width enables us to probe ultrafast transient thermal transport with sub-picosecond temporal resolution. Typically the power per pulse coming out of the laser cavity is approximately 15 nJ and the average power is around 1.3 W. From the Tsunami cavity which generates laser pulses through mode locking, the laser beam passes through an optical isolator to avoid possible reflections to destabilize the laser. The combination of a half wave-plate

31

(HWP) and a polarizing beam splitter forms an adjustable beam splitter that controls the power going into each arm. Generally around 95% of the power from the isolator is sent into the pump arm while the remaining 5% goes into the probe arm. The absolute power level impinging on the sample surface varies widely but is typically around 100 mW from the pump and 15 mW from the probe. The steady temperature rise of the transducer is estimated to be only several Kelvins, which validates the assumption of linear invariant system [52, 53].

The pump beam is modulated by an analog electro-optic modulator (EOM) amplifier (Conoptics 25A) to enable lock-in detection, which chops the pump with a sinusoidal wave [33]. The sinusoidal modulation effectively removes the odd harmonics in the pump beam, therefore removing the need for a resonant filter and significantly enhancing the SNR. The modulation frequency is controlled by a function generator connected to the EOM and normally varies from 1 MHz to 12 MHz. We use a bismuth triborate (BIBO) crystal to frequency double the wavelength of the pump beam from 800 nm to 400 nm. This allows us to use color filters to prevent any scattered pump-light from reaching the detector. A telescope placed after the BIBO crystal adjusts the size of the pump spot on the sample. To zero the noise when the pump beam is blocked completely, an automated beam blocker is placed after the telescope to null the constant offset noise. Then the pump passes through a 10x microscope objective and is focused onto the sample surface.

After passing through the beam splitter, the probe goes through a 4x expander to reduce the beam divergence along the optical path. The variable probe path length is dynamically regulated by a mechanical stage placed after the expander. In our experimental setup, the maximum delay time is around 7 ns. The probe is recompressed to its original size and passes through two cylindrical lenses to correct the inherent astigmatism of the laser spot. The two cylindrical lenses are introduced to correct the beam divergence angle and beam waist position in one dimension so that it matches with the other dimension, thus reducing the spot's astigmatism. Then the probe is focused onto the

32

sample surface coaxially with the pump arm through a 10x microscope telescope. The pump size is allowed to vary while the focused probe spot size is fixed to be approximately 11 μm. Complete overlap between the pump and probe arms is critically important in this experiment to satisfy the model assumptions and for a high SNR. To achieve a good overlap between the two arms, we fix the position of the probe beam and adjust the position of the pump beam until the maximum reflectance signal is obtained.

The periodic pump beam results in oscillations of the sample surface temperature (and its reflectance) in the time domain. The reflectance is encoded in the time-delayed probe beam at the driving frequency. However, since the absolute reflectance of the sample is already very high, the reflected signal also contains components at multiples of the laser repetition rate (80 MHz) from the pump and probe beams that are much stronger than the small changing reflectance signal we wish to extract. The reflected pump beam can easily overwhelm the detector. To avoid this, color filters with selective surfaces are used to separate these two reflected beams of different colors. The reflected probe light carries the transport information and goes through a color filter which effectively blocks the unwanted reflected pump beam. Next, the reflected probe signal is detected by a silicon diode photodetector, whose current depends upon the intensity of the incoming light. Since the generated current from the reflected probe light is typically extremely small (on the order of 1 pA), a trans-impedance amplifier is used to amplify the signal to a usable voltage [33]. Before the signal is sent to the lock-in amplifier, it passes through a low frequency band-pass filter to eliminate the higher-frequency components of the probe arm stemming from the laser repetition rate. The band-pass filter only passes light around the modulation frequency with an adjustable band width which can be set by tuning the time constant in the lock-in amplifier [55]. In our setup, the time constant is typically set to be 30 ms, giving a 10 Hz band width. In addition, the cable length between lock-in amplifier, function generator, and the analog amplifier is shortened to minimize the electromagnetic interference effect introduced by the electrical cables.

During the measurement, a Labview program records the voltage signal from the lock-in amplifier. This signal is directly related to the change in reflectance and temperature of the sample surface. A non-linear least square minimization technique is used to match the Fourier solution with the experimental cooling rate, thus extracting the effective thermal properties being measured. The properties of interest are usually the thermal interface conductance between the transducer film and the substrate and the apparent thermal conductivity of the substrate.

In the following section, we briefly review the diffusive heat transfer model used to extract the transport properties from the experimentally measured reflectance data. We refer interested readers to Dr. Aaron Schmidt's Ph.D thesis [52], Dr. Austin Minnich's Ph.D thesis [33], Kimberlee Collins' master thesis [53], and Maria N. Luckyanova's master thesis [54] for a complete derivation.

2.3 Heat Transport Model

We first review the heat transfer model for heat flow across continuous layered structures and then generalize that to account for the discontinuous nature of the nanodot array structure. The thermal properties of interest are treated as free parameters which are adjusted until the Fourier solution matched with the experimentally retrieved data through a multidimensional nonlinear least squares algorithm.

The thermal response of the sample is described by a thermal transfer function defined as follows [52]:

$$Z(\omega_0) = \frac{\beta Q Q_{probe}}{T^2} \sum_{k=-\infty}^{\infty} H(\omega_0 + k\omega_s) e^{ik\omega_s \tau} \qquad (2\text{-}1)$$

where β is the thermoreflectance coefficient of the transducer film, Q and Q_{probe} are the absorbed pump and probe power, respectively, ω_0 is the pump modulation frequency

set by the function generator, ω_s is the laser sampling frequency (80 MHz), T is the laser repetition period, τ is the delay time, and $H(\omega)$ is the sample frequency response. The thermal transfer function $Z(\omega_0)$ is related to the output of the lock-in amplifier through:

$$Re^{i(\omega_0 t + \phi)} = Z(\omega_0)e^{i\omega_0 t} \tag{2-2}$$

where R and ϕ are the signal amplitude and phase, respectively. Equation (2-2) simply states that the amplitude of the signal is given by the magnitude of the response and the phase of signal is given by the phase offset of the sample response. The real and imaginary parts of the transfer function relate respectively to the in-phase component, X, and out-of-phase component, Y, returned by the lock-in amplifier. The input signal to the lock-in from the photodetector is mixed with a sinusoid to generate those two signal components, which yield the signal amplitude and phase through:

$$R = \sqrt{X^2 + Y^2} \tag{2-3}$$

$$\phi = tan^{-1}(Y/X) \tag{2-4}$$

The following three sub-sections outline the procedure to obtain the thermal frequency response $H(\omega)$ for three different sample structures: continuous film, single dot, and dot array.

2.3.1 Continuous Film Model

The frequency response $H(\omega)$ can be obtained by solving the transient radial heat conduction equation in cylindrical coordinates for a layered structure. The detailed mathematical derivation is given in reference [56] by Carslaw and Jager. Figure 2-2 shows a schematic of the sample, modeled as a multi-layer stack, used in the TDTR experiments.

35
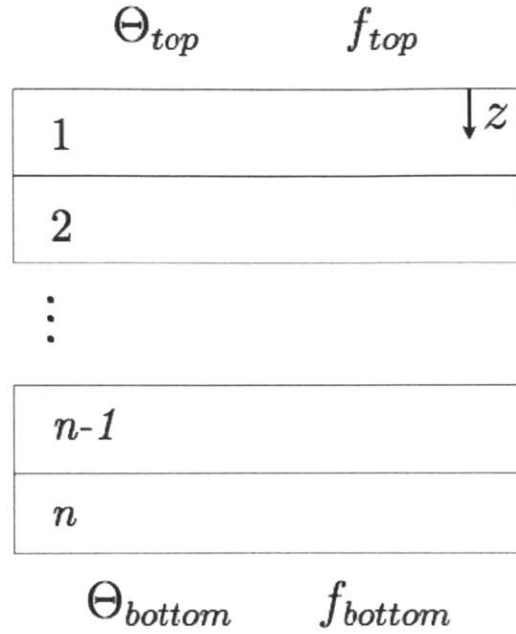
Figure 2-2 Diagram of layered structures used in pump-and-probe experiments [52].

We assign an index to each layer in the stack with the top layer numbered 1 and the bottom layer numbered n. The solution from solving the anisotropic heat equation yields a transfer matrix equation which relates the top surface temperature $\theta_{t,n}$ and heat flux $f_{t,n}$ of the n_{th} layer to the bottom surface temperature $\theta_{b,n}$ and heat flux $f_{b,n}$ of that layer, where t and b denote the top and bottom surfaces, respectively. The relationship is given as:

$$\begin{Bmatrix} \theta_{b,n} \\ f_{b,n} \end{Bmatrix} = \begin{Bmatrix} \cosh(qd) & -\frac{\sinh(qd)}{\sigma_z q} \\ -\sigma_z q \sinh(qd) & \cosh(qd) \end{Bmatrix} \begin{Bmatrix} \theta_{t,n} \\ f_{t,n} \end{Bmatrix} \qquad (2\text{-}5)$$

where σ_z is the layer cross-plane thermal conductivity, d is the thickness of that layer, and σ_z is the cross-plane thermal conductivity. In Eq. (2-5), q is given by $q = \sqrt{\frac{\sigma_r k^2 + i C_v \omega}{\sigma_z}}$, where ω is the periodic laser heating frequency, σ_r is the in-plane thermal conductivity, C_v is the volumetric specific heat capacity, and k is the Hankel transform variable. The effect of radial conduction effect is accounted for in the matrix equation (2-5) through the

introduction of the variable q. Each layer is characterized by three independent properties important to thermal transport: thermal conductivity, heat capacity, and layer thickness. Note that we have omitted the periodic factor $e^{i\omega t}$ while assuming periodic heat transport through the stack.

The transfer matrix for multiple layers with different material properties can be integrated into a single matrix M by simply multiplying the matrix for each layer, as shown by Eq. (2-6) [52]:

$$M = M_n M_{n-1} \cdots M_2 M_1 \tag{2-6}$$

Interfaces between two adjacent layers are incorporated into the matrix formula by noting that the heat flux on either side of each interface should be continuous:

$$f_{b,n-1} = f_{t,n} \tag{2-7}$$

as required by the energy conservation law. Interfaces can be modeled as an imaginary material layer with zero heat capacity and zero thickness. In that limit, Equation (2-5) reduces to:

$$\begin{Bmatrix} \theta_{b,n-1} \\ f_{b,n-1} \end{Bmatrix} = \begin{Bmatrix} 1 & G^{-1} \\ 0 & 1 \end{Bmatrix} \begin{Bmatrix} \theta_{t,n} \\ f_{t,n} \end{Bmatrix} \tag{2-8}$$

where G is the thermal interface conductance (the inverse of thermal boundary resistance). The interface conductance is defined as the heat flux across the interface divided by the temperature difference across it.

Typically the sample consists of three 'layers': the optical-thermal transducer on top, the interface, and the substrate being studied. Combining the three layers relates the temperature and heat flux at the top surface of the sample to the same quantities at the bottom surface of the sample through:

$$\begin{Bmatrix} \theta_b \\ f_b \end{Bmatrix} = \begin{Bmatrix} A & B \\ C & D \end{Bmatrix} \begin{Bmatrix} \theta_t \\ f_t \end{Bmatrix} \tag{2-9}$$

where the subscripts b and t denote the very bottom and top boundaries, and the matrix elements A, B, C, and D are determined by the material properties of each layer through the product of individual material matrices, as given in Eq. (2-6). Two boundary conditions are needed to solve for the surface temperature. Normally the periodic heating at the top boundary is given by the modulated pump beam and the very bottom surface is assumed to be adiabatic since we approximate the substrate as a semi-infinite body. The latter assumption can be easily verified by estimating the thermal penetration depth of the laser beam, which is given roughly by $L_{tp} \approx \sqrt{\frac{\alpha}{2\omega_0}}$, where α is the substrate thermal diffusivity and ω_0 is the pump modulation frequency. In the TDTR setup, the modulation frequency typically varies between 1-15 MHz and the thermal diffusivity is typically on the order of $10^{-5}\,\mathrm{m^2/s}$. Under these conditions, we estimate the thermal wave penetration depth to be approximately tens of micrometers for common substrates. Substrate thickness is usually on the order of 0.5 mm, far exceeding the laser penetration depth, which validates the use of the adiabatic condition at the sample bottom boundary. Equation (2-9) together with the two boundary conditions gives the surface temperature of the sample as:

$$\theta_t = -\frac{D}{C} f_t \tag{2-10}$$

In the Hankel transformed domain, the heat flux boundary condition at the top surface accounting for the Gaussian intensity distribution of the pump beam is given by:

$$f_t = \frac{A_0}{2\pi} \exp\left(-\frac{k^2 \omega_0^2}{8}\right) \tag{2-11}$$

where A_0 and ω_0 are the absorbed pump power and pump beam width, respectively. Substituting f_t into Eq. (2-10) gives the surface temperature in the Hankel transform

domain:

$$\theta_t = -\frac{D}{C}\frac{A_0}{2\pi}\exp(-\frac{k^2\omega_0^2}{8}) \qquad (2\text{-}12)$$

Weighting this surface temperature with the Gaussian probing profile and performing an inverse Hankel transform results in the final frequency response of the sample in real space:

$$H(\omega) = \frac{A_0}{2\pi}\int_0^\infty k(-\frac{D}{C})\exp(-\frac{k^2(\omega_0^2+\omega_1^2)}{8})dk \qquad (2\text{-}13)$$

where ω_1 is the $1/e^2$ probe radius.

To probe phonon MFPs at the nanoscale, instead of a continuous metal film, we use an array of metal nanodots as our optical-thermal transducer. By illuminating the entire dot array and observing the resulting heat transfer, the effective heat transfer length scale becomes the dot diameter rather than the optical laser diameter. That is, we effectively confine the heated area to be within the nanodots. This allows us to probe much shorter length scales, far below the diffraction limit. However, the dot array structure also significantly complicates the heat transfer analysis. In the following two subsections, we briefly review the single dot heat transfer model and the dot array transport model, separately. Interested readers are referred to reference [33] for a detailed derivation.

2.3.2 Single Dot Heat Transfer Model

A schematic of the nanodot array structure used in the spectroscopy experiments is shown in Figure 2-3. In the limit that the dots are far apart from each other, we can approximate that thermal interactions between different dots are negligible. In this single dot picture, the heating and probing profiles are both modeled as a radial step function of the dot diameter w [33]. Carrying out the zero-order Hankel transform of a circular step

function results in $J_1(wk)/k$, where $J_1(k)$ is the first-order Bessel function of the first kind [57]. After replacing the exponential function in Eq. (2-13) with $J_1(wk)$, the final frequency response becomes:

$$H(\omega) = \frac{A_0}{2\pi} \int_0^\infty k(-\frac{D}{c})J_1(wk)^2 dk \tag{2-14}$$

This is the sample response without accounting for the thermal interactions between neighboring dots, which means it is accurate only when the dot separation is large and the dot diameter is small compared with the focused laser spot size.
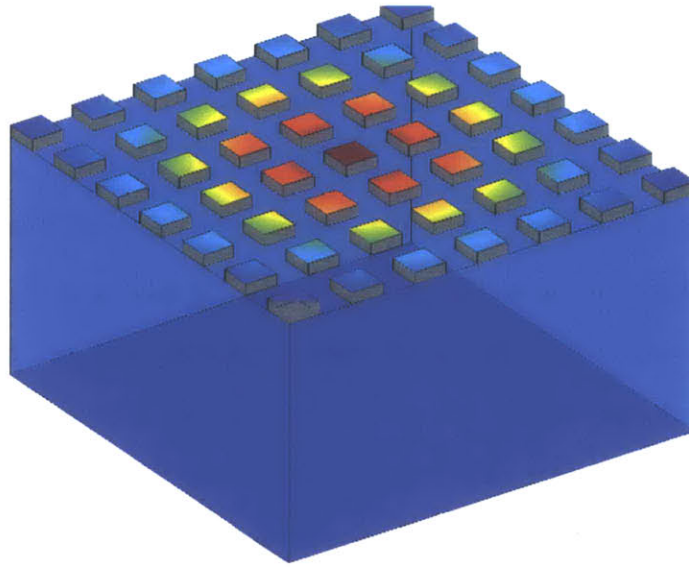
Figure 2-3 Diagram of the dot array structure illuminated by a pump beam with a large diameter [33].

2.3.3 Dot Array Heat Transfer Model

When the separation between neighboring dots is small, the discontinuous nature of the dots and thermal interactions between the dots must be accounted for to yield the correct heat transfer solution. Given the periodicity of the dot array structure, it is easier to perform Fourier transform instead of Hankel transform. Hence a Fourier transform is taken,

which requires the use of square dots rather than circular dots since the former allows us to obtain analytic Fourier series solutions [33]. The dot size in our designed pattern varies in a wide range of length scales and is typically much smaller than the laser spot diameter, resulting in two simplifying approximations. First, heat conduction along the radial direction within the metal dots is assumed to be negligible compared with that along the cross-plane direction. Equivalently, heat is approximated to diffuse only in the cross-plane direction [33]. In addition, the heating and probing laser profiles are approximated as square waves, mimicking the shape of the dot array structure. In reality, the heating and probing profiles are both Gaussian in shape, differing from the square waves. Fortunately, the pump and probe laser diameters in our TDTR setup are approximately 30 μm and 11 μm, respectively, much larger than the dot array period (normally below 2 μm) in the patterned structure. This sharp size contrast between the laser spots and the dots allows us to assume infinitely large laser diameters with uniform intensity distribution [33]. Since the sapphire substrate is non-absorbing to the laser wavelength used in the TDTR system, the approximation of square wave heating and probing profiles is reasonable.

Under these approximations, we repeat the heat transfer derivation process by performing a Fourier transform of the heat equation in the Cartesian coordinates. Compared with the solution in cylindrical coordinates, the difference is mainly in the definition of the parameter q which now becomes [33]:

$$q = \frac{\sigma_{xy}(k_x^2 + k_y^2) + iC_v\omega}{\sigma_z} \tag{2-15}$$

where σ_{xy} and σ_z are the in-plane and cross-plane thermal conductivities, respectively, and k_x and k_y are the Fourier transform variables. After Fourier transforming a square wave heating profile, substituting it into Eq. (2-10), and weighting the surface temperature by another square wave probing profile, the sample's final frequency response becomes [33]:

41

$$H(\omega) = \sum_n \sum_m |X_{nm}|^2 (-\frac{D}{c})_{n,m} \qquad (2\text{-}16)$$

where n and m denote the frequencies $k_x = n\Omega_0$ and $k_y = m\Omega_0$ ($\Omega_0 = \frac{2\pi}{L}$ is the spatial frequency of the dot array structure, where L is the nanodot array period), and X_{nm} are the Fourier coefficients of the square heating wave and are given by [33]:

$$X_{nm} = \begin{cases} w^2/L^2 & n = m = 0 \\ \frac{w/L}{2\pi m j}(1 - \exp(-jm\Omega_0)) & n = 0, m \neq 0 \\ \frac{w/L}{2\pi n j}(1 - \exp(-jn\Omega_0)) & n \neq 0, m = 0 \\ -\frac{(1-\exp(-jm\Omega_0))(1-\exp(-jn\Omega_0))}{4\pi^2 mn} & n \neq 0, m \neq 0 \end{cases} \qquad (2\text{-}17)$$

where w is the dot size and j is the imaginary number $j = \sqrt{-1}$. Note that those constants in Eq. (2-16) have been omitted since the data is normalized when we do the fitting.

We have analyzed the heat transfer model to extract the transport properties for a single dot and a dot array structure. Different shapes of dots are used due to mathematical convenience in those two heat transfer models. However, as pointed out in reference [33], the shape of the dots does not significantly affect the experimental data as long as the dot size is the same. The following section outlines the sample fabrication details, followed by the metal dots thickness calibration. In section 2.6 experimental data of the apparent thermal conductivity of a sapphire substrate is analyzed in detail.

2.4 Sample Fabrication

We used a standard metal lift-off technique to pattern metallic nanodot arrays onto a sapphire substrate. The crystalline sapphire wafers purchased from the MTI Corporation have an area of 12.5 mm^2, and are single-side polished with a c-plane crystalline axis. Sapphire is chosen as the substrate because it is transparent to the laser wavelengths we

use in the TDTR experiment. The bulk thermal conductivity of sapphire at room temperature is around 35 W/mK and the estimated MFPs are in the range of hundreds of nanometers. We lithographically deposit aluminum metallic dots onto the sapphire substrate because aluminum has a high thermoreflectance coefficient. The dots are squares of varying sizes from tens of micrometers down to tens of nanometers, which enable us to probe heat transfer at nanometer length scales.

All the fabrication is done in the Microsystems Technology Laboratory at MIT. To fabricate the sample, deionized water is first used to rinse the original sapphire wafer, followed by a complete blow-dry with nitrogen. After that, we spin-coat a thin layer of the electron beam resist 950K A4 PMMA (polymethyl methacrylate) on top of the wafer at a spin speed of 3500 rpm and a spin time of 50 seconds. This yields an approximately 220 nm thick resist. Following the deposition of the resist, the sample is immediately prebaked on a hot plate preset at 180 °C for about 2 minutes.

The resist needs to be exposed after prebaking so that the designed pattern can be transferred onto the wafer. Before exposure, since sapphire is inherently electrically insulating, we deposit a very thin layer of a conductive metal (either 5 nm Ti or Cr) to avoid the issue of charge accumulation during the lithography process. The ebeam machine Elionix at MIT is used to expose the resist at 125 KeV. The entire pattern, spanning 0.5 mm x 1 mm, consists of closely packed arrays of square dots of different size and spacing.

Since the Elionix automatically does dosage correction, different locations on the pattern are assigned different dosages. Normally the central part of the array has a smaller dosage than the preset, and vice versa for the outer part. PMMA is a positive resist, meaning that the parts exposed by the e-beam are removed after development. After lithography, the thin conductive metal layer is stripped with a 20:1:1 $H_2O:HF:H_2O_2$ solvent bath. Several seconds are enough to remove around 5 nm Ti film. Then we use a 3:1 MIBK:IPA solution to develop the resist for about 2 minutes, followed by an IPA

(isopropyl alcohol) rinse and blow-dry with nitrogen. The pattern is checked under an optical microscope to verify the quality of the lithography process.

Then we deposit a thin aluminum film (around 70 nm) onto the sapphire wafer using e-beam evaporation. The deposition rate is controlled to be approximately 1 Å/sec and the set point of the vacuum pressure is 10^{-6} torr. By analyzing the heat transfer model, we know that the thickness of the transducer film must be within a certain range (usually between 70 nm and 120 nm). The vacuum pressure in the e-beam machine chamber controls the quality of the interface between the metal dots and the sapphire substrate. Higher vacuum (lower pressure) usually gives much better interfaces and vice versa. Thus the deposition process is delayed until the vacuum pressure is at or below 10^{-6} torr. While there is some non-uniformity in the film thickness across the wafer, this non-uniformity is minimal due to both the 0.8 m distance between the crucible containing the desired metal and the wafer and the rotation of the sample holder around the chamber.
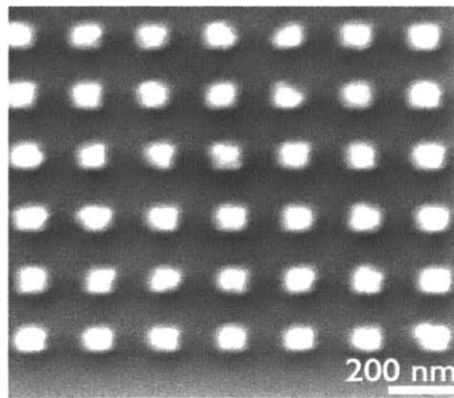
Figure 2-4 Sample SEM image of the fabricated nanostructures (dot size = 90 nm).

Following metal deposition, we use acetone to strip the remaining resist off the sapphire wafer. Soaking the sample in acetone for several hours completely removes all the remaining resist. Finally the wafer is rinsed by IPA after the lift-off process and blown dry with nitrogen. A SEM image of the fabricated nanostructure (heater size = 90 nm) is

shown in Fig. (2-4).

Normally the nanodot array period is twice that of the dot diameter in the fabricated pattern. In the large length scale limit, the dots cool down independently without influence from neighboring dots due to the diffusive nature of thermal transport. Both single dot and dot array heat transfer models are expected to return the same results. However, in another limit where the dot diameter and separation between dots are small, coupling between different dots should be accounted for. This can be easily assessed by estimating the thermal wave penetration depth, which is given by $L_{tp} \approx \sqrt{\frac{\alpha}{2\omega_0}}$ [33, 52-54]. A simple analysis yields a penetration depth of approximately 1 μm in sapphire, which implies that the dot array heat transfer model must be used when length scales become smaller than 1 μm. The dot array model automatically accounts for the interactions between neighboring dots and returns the correct solution when strong coupling is present.

2.5 Thickness Calibration

In the TDTR experiments, knowledge of the metal thickness is critical. 5 nm variation in the thickness would lead to around 5%-10% variation in the apparent thermal conductivity. Quite commonly, the real thickness is a little bit larger than the set point during the metal deposition process. Thus we cannot trust the preset thickness and instead have to determine it independently.

There are several ways to characterize the metal thickness. One useful tool is the Dektak, located in the Exploratory Materials Laboratory (EML) at MIT, a contact surface profilometer which uses a mechanical stylus to determine surface profiles. The resolution of the Dektak reading depends upon the metal film thickness itself. For our nanodot structure the resolution is approximately 1 nm. Since smaller dots would be vulnerable to the force exerted by the mechanical stylus, typically we use the Dektak to determine the thickness of large dots (90 μm). The sample is assumed to have uniform thickness for all

45

the dots of varying sizes, which is validated by the very small pattern area (0.5 mm x 1 mm).

Another way of determining the thickness is by conducting a TDTR measurement on a known film to achieve self-consistent results. For very large dots (90 μm), we expect to recover the bulk substrate thermal conductivity from the measurements when the metal thickness is correct. Thus the thickness can be determined by varying input thickness in the fitting program until the bulk value is obtained. It is also possible to use acoustic echos to determine the metal thickness [52].

2.6 Experimental Results

We lithographically patterned square aluminum metal dots of varying sizes onto a sapphire substrate and determined the metal thickness using a contact surface profilometer. Ideally, the measurement of the varying reflectance signal from an individual dot of different sizes would yield the most convincing claim of the presence of size effects. However, the signal from a single dot is so small as to be undetectable. Thus, square dot arrays are employed to increase the signal. In the patterns used herein, the metal dots occupy only 25% of the sapphire substrate surface area. Since sapphire is nearly transparent to visible light spectrum, any reflectance signal must come from the dots. To offset the small fractional occupation, we increased the pump intensity a bit while decreasing the spot size to 30 μm and slightly increased the power going into the probe arm [33]. This gave us at least 10x SNR for probing the thermal properties. The measurement was done on two different samples at two different modulation frequencies (3 MHz and 12 MHz).

Figure 2-5 shows the measured reflectance signal as a function of the delay times for two different heater sizes. The reflectance amplitude (Fig. 2-5(a)) decays monotonically with respect to the delay between pump and probe after 500 ps. Information about the

46

transport properties of the substrate are contained within this thermal decay which represents the cooling of the dots due to heat flow into and through the substrate.
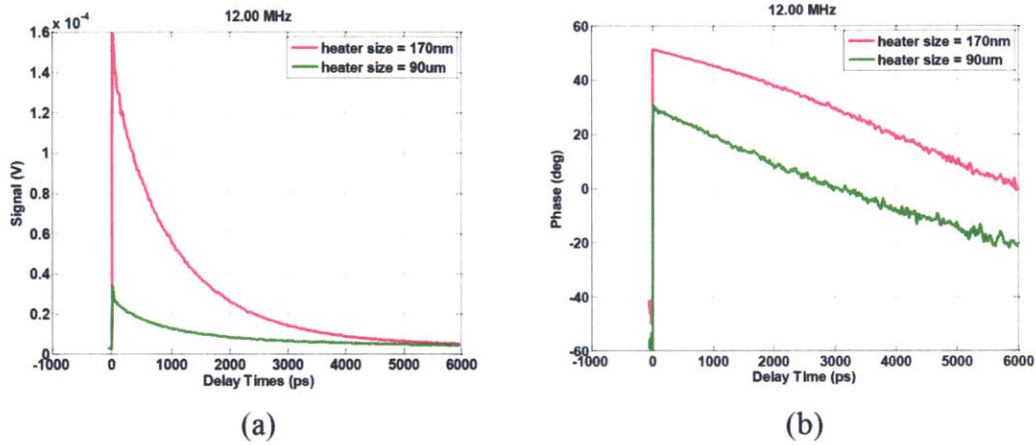
Figure 2-5 (a) Representative trace of the amplitude of the signal from experiment; (b) Representative trace of the phase of the signal from experiment.
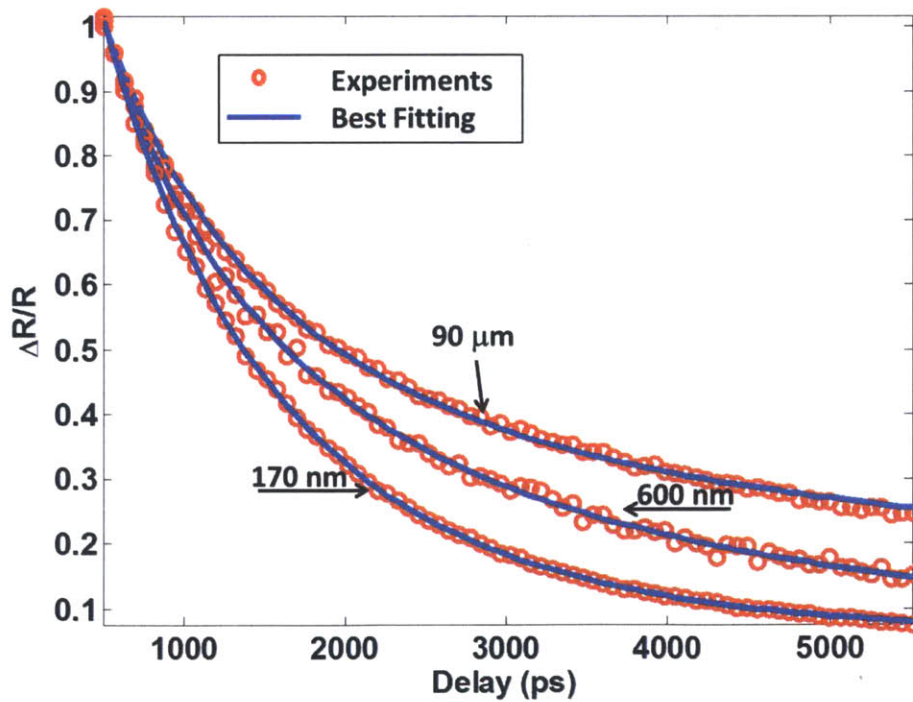
Figure 2-6 Examples of experimental data and fittings based on the Fourier's law.

Figure 2-6 shows experimental data and model solutions for three different length scales (90 μm, 600 nm, and 170 nm). The red dots represent measured data and the blue curves represent the model best fits. The red and green curves are obtained by offsetting the thermal conductivity by ±10%. The agreement between the experimental data and the model fits is quite good for all cases. For large heat source (90 μm), the measured apparent thermal conductivity is around 35 W/mK, the bulk thermal conductivity of sapphire along c-axis at room temperature. This indicates that the transport is in the diffusive regime since the heater size is much larger compared with the phonon MFPs. The presence of size effects is evident for the other two cases. The measured effective thermal conductivities are approximately 27 W/mK and 23 W/mK for the 600 nm dot size and 170 nm dot size, respectively. These values are much lower than the bulk value, indicating the experiments measured an additional thermal resistance for those two length scales.
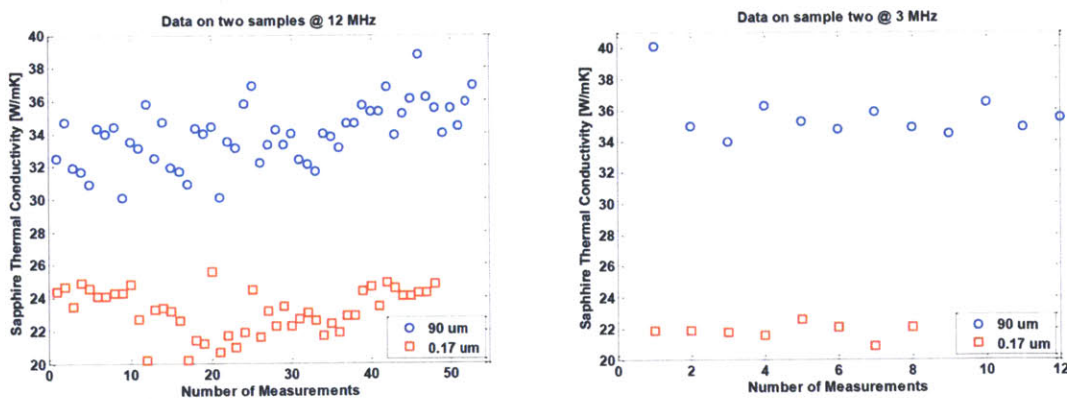
Figure 2-7 Scatter plots of measured sapphire thermal conductivity as a function of heater size at two different modulation frequencies.

Scatter plots of the measured sapphire apparent thermal conductivity as a function of heater size (90 μm and 170 nm) at two different modulation frequencies (3 MHz and 12 MHz) is shown in Fig. 2-7. It is clear that the effective thermal conductivity decreases as the length scale is reduced. In addition, no significant frequency dependence in the

measured thermal conductivity was observed in the experiments.
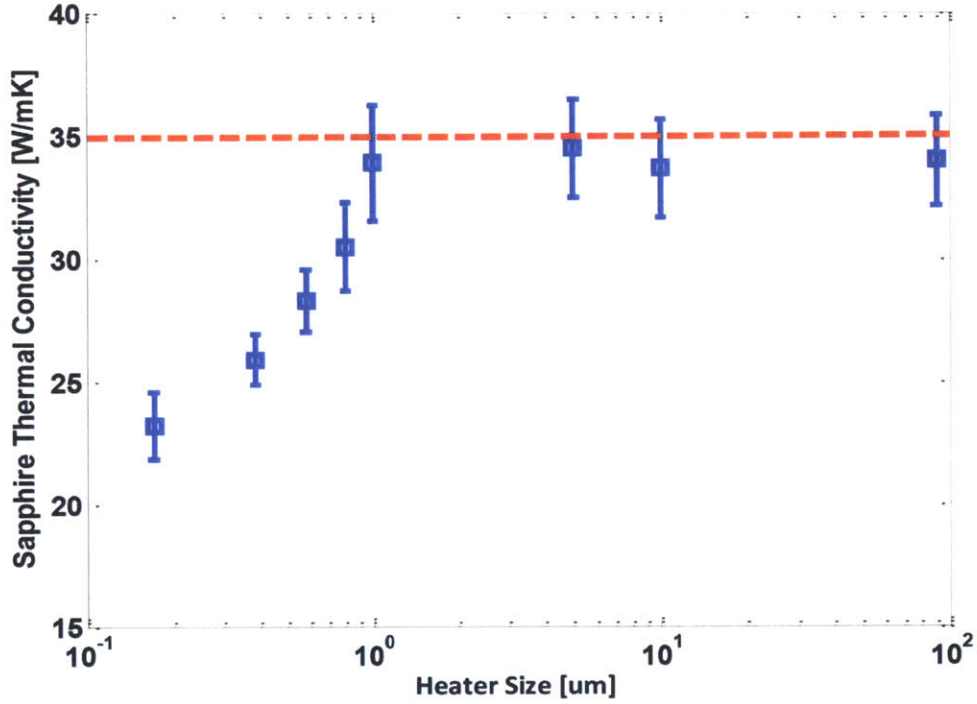
Figure 2-8 Measured sapphire thermal conductivity vs. heater size. Quasi-ballistic transport occurs when the heater size is below 1 μm, which indicates that phonon MFPs in sapphire are in the range of hundreds of nanometers.

The experimentally retrieved average sapphire thermal conductivities over 40 measurements for different length scales are shown in Fig. 2-8. The error bars represent the standard deviations in the measurements. The bulk thermal conductivity of sapphire at room temperature is recovered when the heater size is above 1 μm. In this length scale, diffusive transport dominates the heat transfer process and coupling between neighboring dots is weak. Deviations from the Fourier theory occur when the heater size drops below 1 μm and the heat transfer model returns an effective thermal conductivity much lower than the bulk value, which indicates that the transport becomes quasi-ballistic. The effective thermal conductivity decreases constantly with decreasing heater dimension due to the

increase in the ballistic resistance. Thus we conclude that phonon MFPs in sapphire are in the range of hundreds of nanometers, consistent with measurements made by other investigators [27]. Additionally, phonons with MFPs between 170 nm and 1 μm contribute slightly lower than 50% to the total sapphire thermal conductivity.
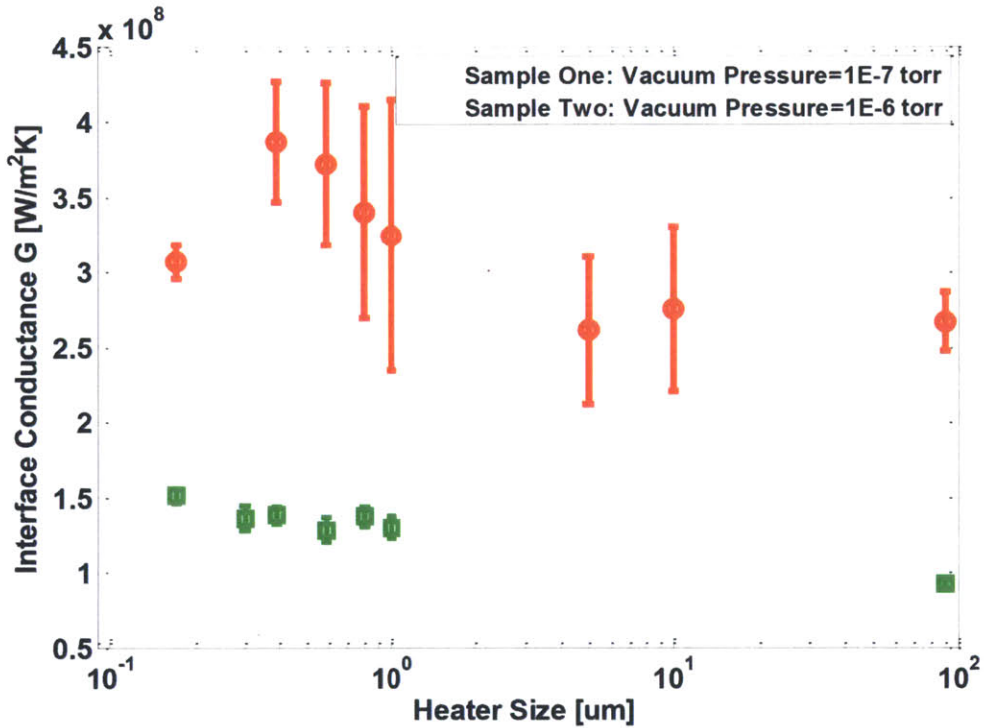
Figure 2-9 Measured interface conductance vs. heater length scales.

Heat transport across the Al-sapphire interface is mainly determined by the unknown thermal interface conductance, G. Thus, we treat the interface conductance as another fitting parameter in the experiments. Figure 2-9 shows the measured interface conductance as a function of length scales for two different samples, for which the metal film was deposited under different vacuum conditions. There is a strong dependence of the interface conductance on fabrication. Generally, the lower the baseline vacuum chamber pressure, the higher the interface conductance. This is expected since lower vacuum pressure usually gives better quality interface. It is observed that the measured data shows a slight

increase in G with respect to decreasing length scales. The variation in G is found to be larger with lower vacuum chamber pressure, which indicates that the non-uniformity of the interface quality is higher under better vacuum conditions.
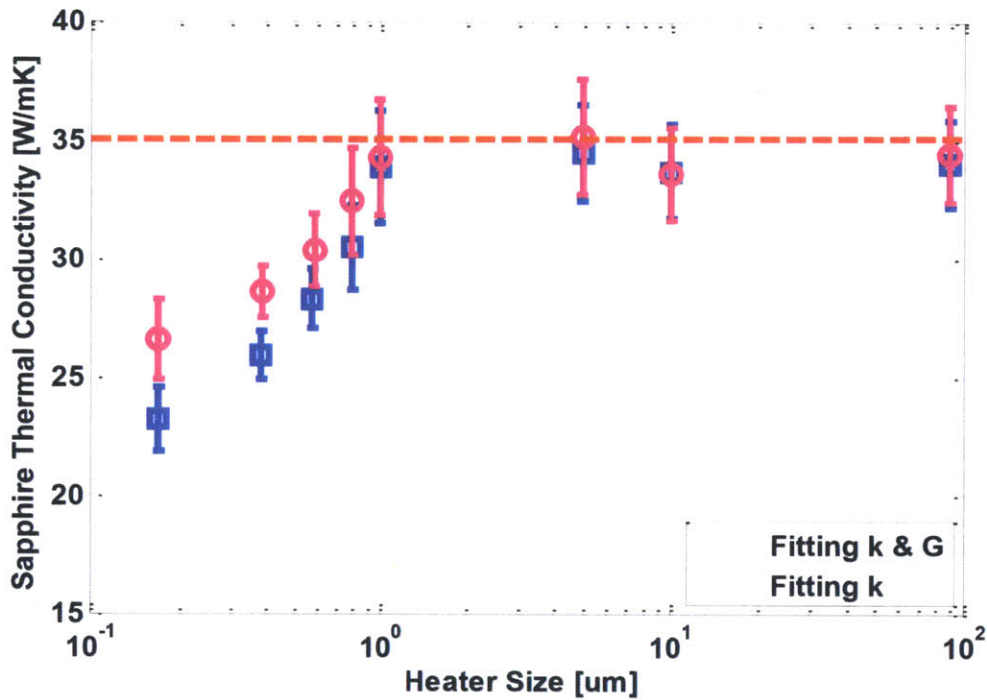
Figure 2-10 Comparison of substrate effective thermal conductivity distribution by fitting both k and G (blue squares) and fitting k only (pink circles).

To examine the impact of the variation in the measured interface conductance on the substrate effective thermal conductivities, the experimentally retrieved reflectance data was fit again to the heat transfer model with a fixed interface conductance measured on the 90 μm dots. This allows us to separate the effect of interface conductance and quasi-ballistic transport in the substrate on the measured substrate effective thermal conductivity [33]. The comparison is shown in Fig. 2-10. The blue squares represent the substrate effective thermal conductivities by treating both the substrate thermal conductivity and interface conductance as fitting parameters, and the pink circles represent

the extracted data by fitting only the substrate thermal conductivity.

For large heater sizes, the effective thermal conductivity does not change significantly after fixing G during the fitting. For small heater sizes, the increase in the effective thermal conductivity implies that the impact of variation in G becomes more pronounced with decreasing length scales. However, the extracted sapphire thermal conductivity with fixed G is still much lower than the bulk value at small heater size (170 nm), which confirms that the size effect is caused by the quasi-ballistic transport in the substrate.

2.7 Summary

In this chapter, we described a new implementation of the time-domain thermoreflectance thermal conductivity spectroscopy technique that enables the experimental study of materials with short MFPs. By optically heating lithographically patterned metallic nanodot arrays, we probed thermal transport properties at length scales down to approximately 100 nm, far below the diffraction limit for visible light. We demonstrated the new implementation by measuring the effective thermal conductivities in sapphire at room temperature using the new technique. The experimentally measured thermal conductivities suggest that MFPs in sapphire are in the range of hundreds of nanometers, consistent with previously reported measurements. The spectroscopy technique confirmed that observations of quasiballistic heat transport contain carrier relaxation information, thus phonon MFP information.

Chapter 3

Multidimensional Modeling using Boltzmann Transport Theory

Knowledge of phonon mean free path (MFP) distribution is critically important for engineering heat transfer at the nanoscale. In chapter 2 we presented the recently developed thermal conductivity spectroscopy technique which can be used to probe MFP distribution down to nanometer scale and demonstrated its potential by measuring the cumulative thermal conductivity of sapphire at room temperature. The observations of quasi-ballistic phonon transport in the experiments allowed us to extract information about phonon MFP distribution in the material being studied. In this chapter, we develop a transport model based on the frequency independent phonon Boltzmann transport equation (BTE) to better understand the effects of different length scales on the heat transport in the quasi-ballistic regime. The simulation geometry, a double-layer structure shown in Fig. 3-1, consists of periodic metallic nanowires sitting on top of a generic substrate. Although the simulation geometry is slightly different from the dot array structure used in the spectroscopy experiments, similar size effects is observed. Two characteristic length scales affecting the thermal transport occur: the heater size w and the array period L. The change in heat transfer is observed by systematically varying these two length scales. Numerical data on the apparent thermal conductivity of a generic substrate at room temperature is

reported by solving the 2D grey transport model under the relaxation time approximation (RTA). The dependence of the thermal interface conductance on the contact size of the nanowire and the substrate is also studied and discussed.
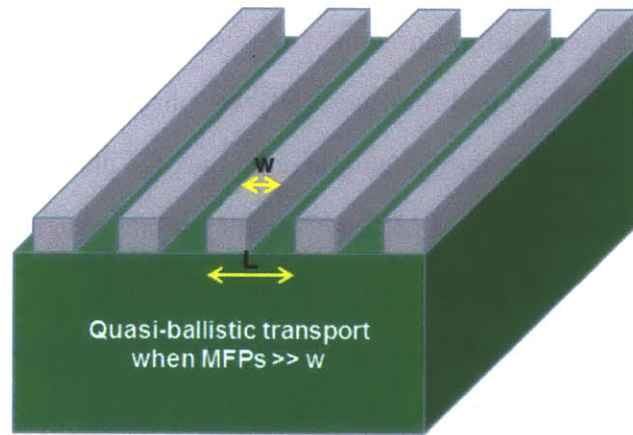
Figure 3-1 Illustration of the simulation domain.

3.1 Background on phonon Boltzmann equation

The phonon Boltzmann transport equation is a differential equation which governs phonon transport by predicting the evolution of the phonon number distribution f in the phase space [18]. Phonons, or quantized lattice vibrations [20, 21], are simulated as individual particles with their phase information completely neglected in the BTE picture. The phonon BTE captures classical size effects precisely when characteristic length scales are much longer than phonon wavelengths (typically on the order of 1-10 nm).

Fourier heat conduction theory captures the transport features in the diffusive transport regime where characteristic length scales are much longer than phonon MFPs. However, in the classical size effect regime where phonon MFPs are comparable with or longer than the characteristic length scales, no phonon scattering occurs and no local thermal equilibrium can be defined [32]. To include the effects of ballistic heat transport, the general phonon BTE needs to be solved. Since the distribution function f depends upon

55

several variables in the phase space, analytic solutions to the BTE can be found only for some simple cases.

Classical size effects have long been examined. Casimir [58] found that the thermal conductivities of crystals have a strong size dependence due to enhanced boundary scattering when the phonon mean free paths are long compared to the characteristic length scale of a finite specimen. Good agreement between his numerical data and reported experimental result by de Haas and Biermasz [59] was observed.

Given the difficulty of obtaining analytic solutions, the phonon BTE has been solved extensively using various numerical methods, including both deterministic and stochastic techniques [60-62], to study phonon size effects. Based on the analogy to photons, Majumdar et $al.$ [60, 63] derived an equation of phonon radiative transfer (EPRT) to describe thermal transport in dielectric thin films, which serves as a good starting point in terms of applying the BTE to heat transfer at short length scales. The EPRT was solved to study phonon transport in thin films of diamond for a wide range of Knudsen numbers (Λ/L_c, MFP divided by film thickness) and an expression of the thin film effective thermal conductivity was obtained for the Fourier diffusion theory to be mathematically applicable. Chen [32] predicted that the heat transfer from a nanoparticle into its surrounding host medium is significantly suppressed compared to the solution of the Fourier law-based heat conduction equation. Based on the phonon BTE, Chen et $al.$ [64-66] developed models for both the in-plane and cross-plane superlattice (periodic stacks of constituting thin films) thermal conductivity and studied the effects of film thickness and interface conditions on the thermophysical properties of superlattices. He observed that partially specular and partially diffuse interfaces gave good agreement between the BTE solution and experimental data on GaAs/AlAs superlattices.

To reduce the huge computational expense required to solve the BTE, Chen [67, 68] proposed to decompose phonons into diffusive and ballistic groups and derived the Ballistic-Diffusive-equation (BDE). The phonon BDE substantially improves the

computational efficiency and better approximates the phonon BTE compared with heat conduction equation and Cattaneo equation in the quasi-ballistic transport regime. In a subsequent work, Narumanchi *et al.* [69] examined the effects of boundary scattering and heat source localization on the thermal transport around an unsteady small hot spot by solving the grey phonon BTE with a finite volume method (FVM). They found significant discrepancies in the prediction of peak temperature rise and thermal response time from the BTE and Fourier's diffusion theory. Another study by Murthy *et al.* [70] substantially improved the accuracy of the FVM through decomposition of phonon intensities into a ballistic component and an in-scattering component, where the former was solved by a ray-tracing scheme and the latter was solved by an unstructured FVM, respectively.

The phonon BTE also allowed systems of greater complexity to be studied, such as nanocomposites, i.e. complex solid materials which include structures with nanoscale dimensions. Nanocomposites have been shown to have significantly reduced lattice thermal conductivities, thus enabling us to potentially improve thermoelectric performance. Yang *et al.* [71] studied the size and volumetric fraction dependence of the thermal conductivity of periodic two-dimensional nanocomposites consisting of silicon nanowires embedded in germanium host medium. Following that work, Yang *et al.* [72, 73] applied the phonon BTE to explore the transport property of silicon-germanium nanocomposites with silicon nanowires and tubular nanowires in a germanium matrix. They found that the additionally introduced surface scattering by the tubular nanowires results an even lower effective thermal conductivity compared with simple nanowires. The phonon BDE was further developed to account for multidimensional thermal transport by Yang *et al.* [74] and applied to study the effects of boundary conditions and nanoscale heat source size on the heat transport of a 2D rectangular structure. Results of the phonon BDE were compared with predictions from both the multidimensional phonon BTE and Fourier diffusion theory. To simplify the calculations, many studies assumed frequency averaged properties. Unfortunately, phonon MFPs depend strongly upon the vibrational frequency

and polarization.

To account for the non-linear phonon dispersion and frequency dependent phonon MFPs, Minnich *et al.* solved the one-dimensional spectrum dependent phonon BTE for a double-layer structure composed of aluminum metal film on top of a silicon substrate to validate observations of quasi-ballistic transport help extract information about the MFP distribution [75]. Frequency dependent interface properties were incorporated to take into consideration the difference in dispersion relation of the two constituting materials [75]. In the following section, we develop a multidimensional transport model based upon the phonon BTE to simulate heat transport in a periodic nanostructure composed of nanowire array sitting on a generic substrate and observe the effects of different length scales on the effective thermal conductivity of the substrate when characteristic length scale approaches phonon MFPs. Our multidimensional model follows the derivation in reference [75] and is detailed in the next section.

3.2 Multidimensional Transport Model

The full, spectrum dependent phonon Boltzmann transport equation is shown as [18]:

$$\frac{\partial f_\omega}{\partial t} + \vec{V_\omega} \cdot \nabla f_\omega = f_{collision} \tag{3-1}$$

where f_ω is the spectral phonon number distribution function, $\vec{V_\omega}$ is the group velocity, and $f_{collision}$ is the collision term. The distribution function f_ω depends upon the particle frequency ω, position $\vec{r}$, and propagation direction (θ, ϕ). The difficulty associated with solving the BTE stems from the high dimensionality of the distribution function f_ω in the phase space. At each spatial point, f_ω is a function of the local phonon propagation direction, which spans the whole 4π solid angle. Therefore, in order to numerically solve the BTE, both the simulation domain and the local solid angle need to

58

be discretized separately. The term $f_{collision}$ accounts for various phonon scattering mechanisms during thermal transport and typically consists of nested integrals with unknown distribution function f inside the integrand, and poses additional difficulties for solving the governing BTE.

In reality, transport properties, including group velocity, density of states, and phonon lifetimes, are strong functions of phonon modes and polarizations [29]. Due to computational limitations, frequency averaged properties (or grey properties) are used in multidimensional simulations. In this study we solve the grey phonon BTE under the relaxation time approximation (RTA) [76], which can be written as:

$$\frac{\partial f}{\partial t} + \vec{V} \cdot \nabla f = -\frac{f - f_0}{\tau} \tag{3-2}$$

where f_0 is the local equilibrium distribution function, and τ is the averaged phonon lifetime over all the phonon modes. The negative sign indicates that thermal system tends to equilibrium states after being perturbed. For a system at equilibrium, the temperature is well-defined and f_0 follows the Bose-Einstein distribution [18]:

$$f_0 = \frac{1}{\exp\left(\hbar\omega / k_B T\right) - 1} \tag{3-3}$$

where $\hbar$ is Planck's constant divided by 2π, ω is the phonon frequency, k_B is the Boltzmann constant, and T is the absolute temperature. The chemical potential is neglected in Eq. (3-3) since it is zero for phonons. The RTA significantly reduces the computational complexity associated with the scattering term. The following several sub-sections proceed with the RTA to develop a multidimensional grey BTE model used to simulate quasi-ballistic phonon transport in the proposed structure shown in Fig. 3-1.

3.2.1 Phonon Intensity

Instead of solving the distribution function directly, we solve the directional phonon intensity defined as [60]:

$$I = \frac{1}{4\pi} \sum_p \int_0^{\omega_{m,p}} \hbar\omega f_\omega D(\omega, p) V_\omega d\omega \tag{3-4}$$

where $\hbar\omega$ is the phonon quanta energy, $D(\omega, p)$ the density of states at a particular frequency, V_ω is the spectral group velocity, and the summation is over all polarizations p. If we multiply the original BTE by $\hbar\omega f_\omega D(\omega, p) V_\omega$, integrate over all the phonon frequencies, and sum over all the branches, the phonon intensity I then bears the same form as f_ω:

$$\frac{\partial I}{\partial t} + \vec{V} \cdot \nabla I = -\frac{I - I_0}{\tau} \tag{3-5}$$

Similar to the frequency-averaged phonon number distribution function f, the phonon intensity I strongly depends upon position, time, and angle of propagation. As discussed before, different methods have been applied to solve the BTE, including discrete ordinate method, Monte Carlo technique, and the Finite Volume approach, to solve the phonon BTE. In this study the discrete ordinate method is chosen to solve the 2D phonon BTE together with Gauss-Quadrature to integrate properties over the 4π solid angle. Finite difference method is implemented to perform both temporal and spatial discretization in the BTE. Due to the restriction posed by the boundary conditions, the discretized BTE form depends upon the phonon propagation direction and is sketched in Fig. 3-2, where θ and φ are the polar and azimuthal angles, respectively, $\mu = \cos\theta$ is the directional cosine, and η is defined as $\eta = \sin\theta\cos\varphi$.

Generally backward difference is taken when phonons travel along the positive direction, and vice versa. For example, the discretized equation for the quadrant $\mu <$

$0, \eta > 0$ is given by:

$$\frac{I_{i,j,n,m}^{k+1}-I_{i,j,n,m}^{k}}{\Delta t} + V\mu \frac{I_{i+1,j,n,m}^{k}-I_{i,j,n,m}^{k}}{\Delta x} + V\eta \frac{I_{i,j,n,m}^{k}-I_{i,j-1,n,m}^{k}}{\Delta y} = -\frac{I_{i,j,n,m}^{k}-I_{i,j,0}^{k}}{\tau} \qquad (3\text{-}6)$$

where i, j, n, m, k are the x, y, μ, η, time indices, respectively, $I_{i,j,n,m}^{k}$ is the phonon intensity at a specific point (i, j, n, m) in the phase space and time k, and $I_{i,j,0}^{k}$ is the equivalent equilibrium intensity at time k. The discretized transport equation for other propagation directions can be written down similarly. This explicit scheme is used to propagate in time until the expected simulation time is reached.
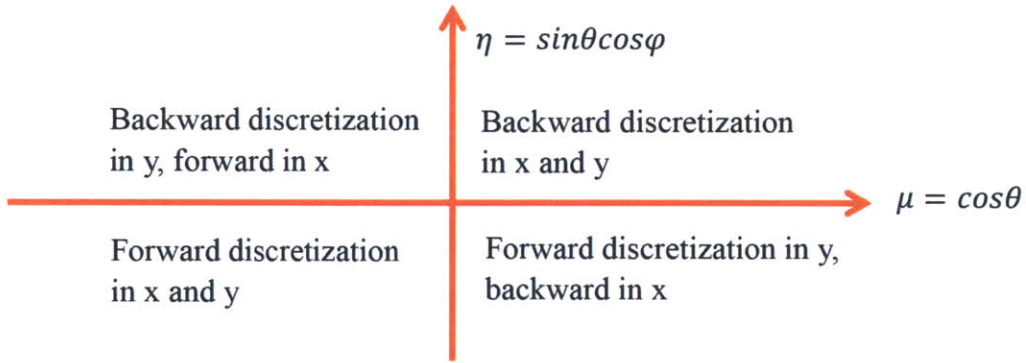
Figure 3-2 Choice of the finite difference method for different phonon traveling directions.

Following the discretization of the phonon BTE using finite difference, interface and boundary conditions need to be specified. The interface and boundary conditions used in the simulations are consistent with experimental conditions in the spectroscopy experiments discussed in chapter 2 and outlined in the following two sub-sections.

3.2.2 Interface Condition

Calculating heat transport across interfaces requires knowledge of interface properties, including the interface transmittance and reflectance. Practically, phonons are very

sensitive to interface qualities, which can greatly affect phonon transmittance across an interface. Currently, no generic model to compute the interface properties exists for arbitrary interfaces. Swartz *et al.* [38] gave a thorough review of thermal boundary resistance studies. Both diffuse mismatch model (DMM) [38, 77] and acoustic mismatch model (AMM) [38, 78] have been developed, but neither of them capture the physics of thermal transport across generic interfaces completely. The AMM assumes that no scattering but specular reflection occurs around the interface while the DMM postulates that any phonon incident on the interface experience diffuse scattering. The DMM model further assumes that phonons leaving the interface have no relation to where they came from. Generally, the AMM applies better to clean and defect free interfaces while the DMM is a better approximation for rough, imperfect interfaces. In this simulation, we implement the DMM to describe the thermal transport across the nanowire/substrate interface.

Phonons incident on an interface have finite probabilities to either transmit the interface or being reflected by the interface. On either side of the interface, three groups of phonons are present: the incident component, the reflected component, and the transmitted component. To calculate the interface transmittance, energy conservation needs to be satisfied. The first law of thermodynamics ensures that:

$$R + T = 1 \tag{3-7}$$

where R and T are the reflectance and transmittance on either side of an interface, respectively. Under thermal equilibrium, the net heat flux across an interface is zero, as required by detailed balance [18]. The detailed balance relates the transmittances on both sides to be:

$$T_{21} = \frac{c_1 v_1}{c_2 v_2} T_{12} \tag{3-8}$$

where T_{12} is the transmittance from side 1 to side 2, T_{21} is the transmittance from side 2 to side 1, and C_i and V_i (i=1, 2) are the volumetric specific heat capacities and speed of sound, respectively. Phonon coupling around interfaces may be very strong. Fox example, a transverse acoustic (TA) phonon on side 1 might become a longitudinal acoustic (LA) phonon on side 2 after transmission. In this study mode conversion is suppressed when treating heat transport across the interface to simplify calculations.

We first assign one reasonable number to the reflectance of phonons from side 1 back to side 1 R_{12}. The energy conservation Eq. (3-7) yields the transmittance from side 1 to side 2 T_{12}. Once T_{12} is obtained, the DMM gives the transmittance from side 2 to side 1 T_{21}. Similarly, R_{21} is computed from energy conservation through (3-7): $R_{21} = 1 - T_{21}$. With the given interface reflectance and transmittance, boundary conditions are discussed in the next section.

3.2.3 Boundary Conditions

The periodicity of the simulation geometry significantly simplifies the calculation by allowing us to simulate one period of the nanostructure. Given the periodicity of the structure, periodic boundary conditions are used for the two sides of the substrate. To implement that, we use specular reflection boundary condition. The substrate is sufficiently thick and is modeled as a semi-infinite body, which indicates adiabatic wall boundary condition is applied. All the other boundaries are modeled as adiabatic walls, consistent with experimental conditions in the TDTR spectroscopy experiments [75]. Particularly, specular reflection is used to satisfy the adiabatic wall requirement. To summarize, all the boundaries are modeled adiabatic with specular reflection.

3.2.4 Equivalent Equilibrium Intensity, Temperature, and Heat Flux

The term I_0 in the BTE corresponds to a locally thermalized state in the transport and is referred to as 'equivalent equilibrium intensity'. The thermalized state is an imaginary state which is reached by adiabatically relaxing phonons to a virtual equilibrium state. The equivalent equilibrium intensity adds difficulty to solving the BTE since it couples different phonon modes. The highly non-equilibrium quasi-ballistic transport poses challenge to define local thermodynamic temperature. Instead of computing the local equilibrium temperature which does not exist, the equivalent equilibrium temperature is calculated based on the equivalent equilibrium phonon intensity, which is a measure of the local phonon intensity averaged in all directions.

Numerically, a two dimensional Gaussian quadrature is used to discretize the 4π (θ, ϕ) solid angle into many angle points and obtain the corresponding weights for each discretized direction. In particular, we discretize the polar angle θ into n points and the azimuthal angle ϕ into m points. Then the relevant weights ω_n and ω_m^* are calculated for each discretized direction and satisfy $\sum_n \sum_m \omega_n \omega_m^* = 2\pi$ [74]. The equivalent equilibrium intensity is computed by averaging the intensities over the solid angle:

$$I_0^k(x, y, t) = \frac{1}{2\pi} \sum_n \sum_m I^k(x, y, \theta, \phi, t) \omega_n \omega_m^* \qquad (3-9)$$

where $I^k(x, y, \theta, \phi, t)$ is the directional phonon intensity at (x, y) along the direction (θ, ϕ) at time t. As a measure of the local energy density, the equivalent equilibrium temperature (or thermalized temperature) is defined as:

$$T(x, y, t) = \frac{4\pi}{cv} I_0^k(x, y, t) \qquad (3-10)$$

The local heat flux is obtained by simply integrating and weighting the component of phonon intensities along the desired direction. For example, if the cross-plane direction is

defined as x, the heat flux along this direction is given by:

$$q_x(x, y, t) = \frac{1}{2\pi} \sum_n \sum_m I^k(x, y, \theta, \phi, t) * \mu * \omega_n * \omega_m^* \qquad (3\text{-}11)$$

where μ is the polar angle. Similarly, the heat flux distribution along the in-plane direction can be written down as:

$$q_y(x, y, t) = \frac{1}{2\pi} \sum_n \sum_m I^k(x, y, \theta, \phi, t) * \sqrt{1 - \mu^2} * \cos(\phi_m) * \omega_n * \omega_m^* \qquad (3\text{-}12)$$

3.2.5 Stability Issue

We use an explicit scheme to march in time during the simulation. As a result, stability issue needs to be considered. To ensure stability, the time step needs to be sufficiently small and is restricted by the following relation [74]:

$$\Delta t < \frac{\Delta x}{V} \qquad (3\text{-}13)$$

where Δx is the minimum spatial step size, and V is the phonon propagation speed. The spatial step is normally chosen to be one tenth of the minimum phonon MFP, as required by the accuracy of the simulation results. This poses a big challenge in solving the spectral phonon BTE because typically the minimum MFP in real materials is approximately 1 nm, which requires the spatial step to be extremely small (on the order of 0.1 nm). The computational cost associated with such small spatial step is very large, resulting in frequency averaged properties to be used in the BTE model. To guarantee both stability and accuracy, the time step given by Eq. (3-13) is typically divided by a safety factor which is specified to be much greater than unity.

3.2.6 Simulation Details

The periodicity of the proposed structure in Fig. 3-1 reduces the simulation domain to consist of one metal nanowire heater on a generic substrate. Initially a temperature pulse is applied onto the heater to approximate the heating effect induced by laser pulses in the ultrafast optical experiments. This driving force excites phonons in the heater which gradually traverse the interface, resulting in heat transport in the underlying substrate. To simplify the calculation, the electron-phonon interaction is neglected in the simulation. After initialization, the transient 2D BTE is solved with specular reflection boundary condition and diffuse scattering interface condition at the dot-substrate interface. The surface cooling rate of the heater is recorded during the simulation. The effective thermal conductivity of the substrate is fitted by matching the Fourier solution with the BTE data. This gives the effective thermal conductivity distribution vs. length scales. The size and temporal dependence of the interface conductance G are also studied from the BTE simulation. The sensitivity of the surface temperature to both the substrate thermal conductivity and the interface conductance was carried out. We observed that the surface temperature is more sensitive to the substrate thermal conductivity if the bulk thermal conductivity of the substrate is low. Therefore, a generic substrate with a low bulk thermal conductivity is used in this study. Table 3-1 lists the material properties of both layers used in the simulation. To compromise computational cost, the input phonon MFP of the generic substrate is averaged over the entire phonon spectrum and chosen to be 100 nm.

Table 3-1 Material properties used for the nanowire and the generic substrate.

Material	Thermal Conductivity (W/mK)	Volumetric Heat Capacity (J/m³K)	Speed of Sound (m/s)	Phonon MFP (nm)
Nanowire	100	2.35E6	3000	42
Substrate	50	1.0E6	1500	100
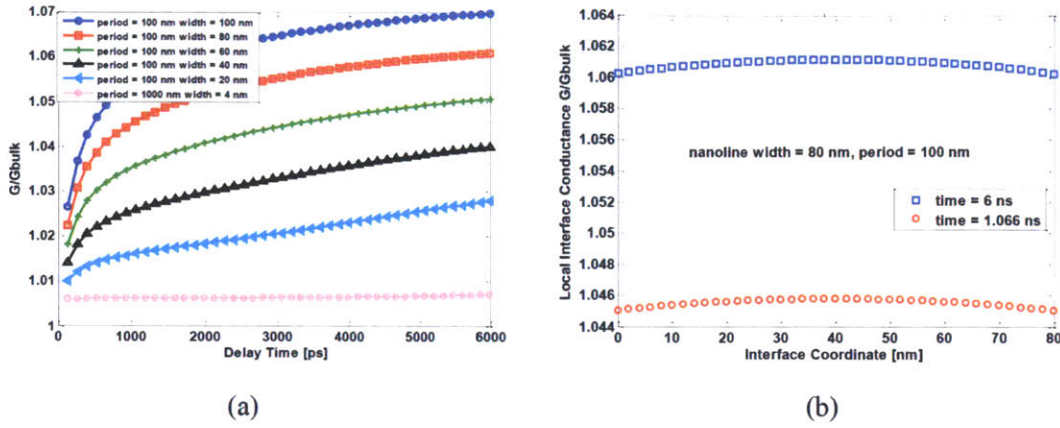
Figure 3-3 (a) G vs. length scales and time; (b) local interface conductance distribution. In both graphs, G_{bulk} is calculated from the DMM model.

3.3 Results and Discussion

Figure 3-3(a) shows the size and temporal dependence of the averaged thermal interface conductance for a variety of heater sizes at two different array periods: 100 nm and 1000 nm. The reference interface conductance G_{bulk} is predicted from the DMM model. Under a fixed period, G is reduced with decreasing heater size. When the heater size becomes extremely small under a large period compared with the phonon MFP, the calculated G from the BTE approaches the solution of the DMM model. In addition, G increases slowly with time, which is not yet fully understood. The overall variation of G from Fig. 3-3(a) is within 7% for all the simulated length scales. Thus, we consider the interface conductance to be constant and only fit the substrate thermal conductivity. The spatial dependence of G for heater size 80 nm and period 100 nm at two different simulation times is shown in Fig. 3-3(b). The local interface conductance peaks around the center of the interface.

Figure 3-4(a) shows some sample fittings of the heater surface temperature for several different geometric configurations. As expected, the effective conductivity

becomes smaller while gradually reducing the heater size under a constant array period. This decrease in the apparent thermal conductivity results from the increase in the ballistic resistance of the quasi-ballistic transport at shorter length scales [27, 32].

(a)   (b)
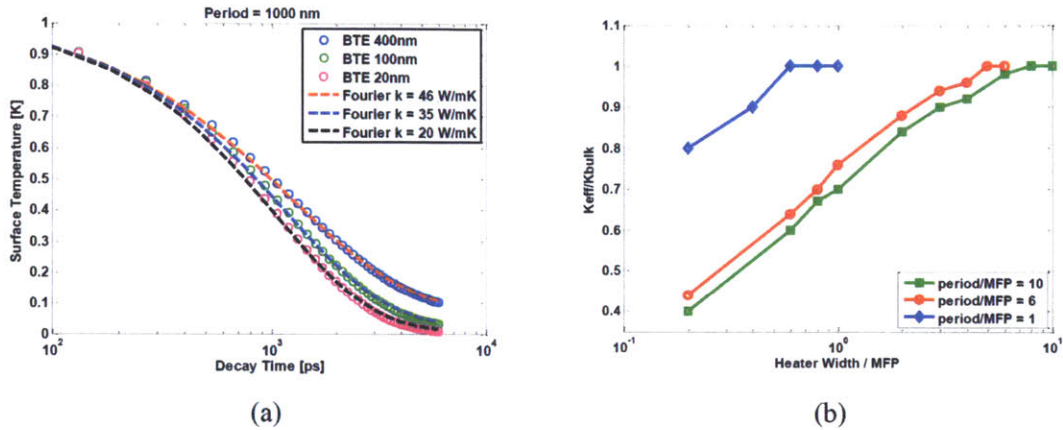
Fig. 3-4 (a) Sample fitting curves; (b) normalized effective thermal conductivity vs. nanoline width and period.

The normalized effective thermal conductivity as a function of length scales is displayed in Fig. 3-4(b). The x coordinate is the inverse of Knudsen number which is defined as $K_n = \Lambda/L_c$, where Λ and L_c are the substrate phonon MFP and the heater size specifically for our applications here. To better understand the transport, we start with a simple case where the period is long compared with the phonon MFP (period/MFP = 10). When the heater size equals the period, it is effectively a continuous film covering the substrate, which indicates the heater size can be considered to be infinitely large. Sufficient scattering occurs after phonon transmission from the heater into the substrate, thus resulting in diffusive transport in the substrate [32, 33]. In such case the fitting recovers the bulk thermal conductivity of the substrate. Then we gradually reduce the heater size but keep the period unchanged. At some point, the heater size d becomes comparable to the phonon MFP and quasi-ballistic transport around the interfacial region starts contributing to the transport in the substrate [33]. The ballistic resistance at this point

68

is relatively small, though. Consequently, the fitting returns an effective thermal conductivity which is only slightly lower than the bulk value. As we further reduce the heater size such that the heater dimension becomes much smaller than the substrate phonon MFP, ballistic transport starts to dominate, resulting in a significantly increased ballistic thermal resistance, which in turn leads to a substantially decreased effective thermal conductivity compared with the bulk thermal conductivity. When the heater size approaches zero, the effective thermal conductivity asymptotes zero.

Practically two important length scales are present in the nanoline-substrate structure: the heater size and array period. Transport becomes more complicated in the limit that the period becomes comparable or even shorter than the phonon MFP (for example, period/MFP = 1). This implies naturally that the heater size must also be comparable with the MFP. For the film case (i.e. heater size = array period), the transport is still diffusive, which again returns the bulk thermal conductivity. When the heater size becomes small relative to the period, we compare two different cases: same heater size with two different periods (a short period and a long period). Figure 3-4(b) shows that the effective thermal conductivity is lower for a longer period, which suggests phonon scattering in the substrate be less effective in the case where the period is much longer compared with the MFP. Under the same heater size, the ballistic resistance associated with a short period turns out to be lower than that associated with a long period. As a result, the effective thermal conductivity is in general higher for a shorter period with the same heater dimension.

3.4 Summary

In this chapter, we studied the quasi-ballistic transport numerically by solving the multidimensional grey phonon Boltzmann transport equation using discrete ordinate method. Frequency averaged properties were used as input into the BTE and interface properties were addressed by the diffuse mismatch model. We found that two geometrical length scales (i.e. heater size and array period) significantly affect the heat transport in the substrate, and consequently the effective thermal conductivity of the substrate. The model routinely predicted a lower interface conductance for a smaller heater dimension, but the overall variation of the interface conductance across a wide range of length scales was found to be very small (within 7%).

Chapter 4

Simulating Heat Transport with Monte Carlo Method

Chapter 3 developed a multidimensional thermal transport model based on the phonon Boltzmann transport equation (BTE) to study heat transport at the nanoscale. Through simulations across a range of length scales, we observed the effects of quasi-ballistic transport on the effective thermal conductivities of a generic substrate. Frequency averaged phonon MFP was used to reduce the computational cost in the 2D calculation. However, in real materials, the phonon MFPs span several orders of magnitude and cannot be represented by any single averaged number. In this chapter we incorporate frequency dependent phonon properties by solving the general BTE using a stochastic "variance reduced Monte Carlo" (VRMC) [79, 80] method. Compared to the conventional MC technique, variance reduced MC method allows us to extract very small signals from the numerical simulations. The developed multidimensional spectrum dependent heat transfer model is applied to the nanostructure composed of metallic nanodot array on a silicon substrate, mimicking the experimental structure. Ensemble average is implemented to obtain clean and smooth signals from the calculations. While in this chapter phonon lifetimes from empirical correlations are utilized, future work will incorporate lifetime

data calculated from first-principles density functional theory (DFT) [29].

Another motivation for this study originates from inverting the experimental spectroscopy data to precisely reconstruct the phonon MFP distribution [36]. In the spectroscopy experiments, effective thermal conductivities were measured as functions of characteristic length scales, i.e. heater sizes. MFPs are roughly inferred by assuming phonons with MFPs longer than heater size do not contribute to heat transport [13, 26]. Unfortunately, the heater size is not an accurate cutoff length scale. Accurate reconstruction of MFPs from experimental data requires a spectral heat flux suppression function which can be obtained from quasi-ballistic phonon transport simulation [36].

In the following two sections, a short review of the applications of MC method to heat transport and the details of implementing variance reduced MC simulation are outlined. Preliminary simulation results and relevant discussions are presented in section 4.3.

4.1 MC Background

As shown in chapter 3, the phonon distribution function depends upon several variables in the phase space and is generally difficult to solve. Solving the full Boltzmann transport equation numerically by a deterministic approach requires huge amount of time and computer memory, and thus is not practical. Nonetheless, phonon MFPs depend strongly on phonon modes [29, 81, 82] and frequency dependent properties must be used to correctly predict and understand the strong size effects which occur in real transport processes.

In the past, direct simulation Monte Carlo (DSMC) methods incorporating the phonon spectrum [83-85] have been used to solve the full phonon BTE. In the DSMC method, a large number of phonons are simulated as individual particles each with their own transport properties and their phase information is completely neglected in this

particle picture. Compared with directly solving the BTE, MC simulations can easily account for real phonon dispersion relations and are more favorable for simulating arbitrary structures. The results of MC method approach those of the BTE when large numbers of phonons are simulated in the structures of interest. By comparing MC results to low temperature experimental data, Klitsner *et al.* [83] analyzed the impact of surface specularity and the effect of thermometers placement on measurements of heat flow and thermal conductivity of polished single crystalline silicon in the ballistic limit. When modeling heat conduction along 1D linear array of cells, Peterson [84] accounted for the spectrum-dependent phonon properties by assuming a Debye dispersion relation. He found that solutions from the MC method matched well with analytic predictions. Although the dependence of phonon MFP on frequency is neglected in his study, this serves as a good starting point to incorporate spectral properties in MC calculations. Mazumdar and Majumdar [85] presented a more comprehensive transport model based on the MC method that considered the nonlinear phonon dispersion and interactions between longitudinal and transverse acoustic phonons. For silicon thin films with and without doping, the simulation results agreed well with experimental data.

Later Chen *et al.* [86] developed a genetic algorithm to treat both the normal and umklapp phonon scattering in the MC model and applied it to the calculation of silicon nanowire thermal conductivities. When the nanowire diameter drops below 20 nm, there were significant differences from the calculations using the bulk dispersion and those using the nanowires' dispersions solved from elastic wave theory, and the results using the nanowire dispersion yielded better agreement with experimental data. Tian *et al.* [87] found the thermal conductivity of the compacted nanocomposites consisting of silicon and germanium nanowire mixtures were reduced to half the value of silicon nanowire embedded in a germanium host. Jeng *et al.* [88] focused on implementation of periodic boundary conditions in the DSMC model and applied it to calculate the properties of Si-Ge nanocomposites. The calculated thermal conductivity was below the alloy limit and

qualitatively agreed with experimental data on Si-Ge nanocomposites. Hao *et al.* [62] investigated size effects of a 2D porous silicon with aligned pores by applying periodic boundary condition and accounting for the frequency and temperature dependence of the phonon lifetimes. The size effects were significant even when the pore size was larger than the averaged silicon phonon MFP, which points out the importance of considering the phonon spectrum to yield accurate results.

Although the DSMC method is a suitable technique to solve the general phonon BTE, some limitations which restrict its use exist. When the temperature difference across the simulation domain is large, DSMC normally gives a good signal to noise ratio (SNR). Unfortunately, if the temperature difference is extremely small, results from DSMC typically become very noisy. In this case, large numbers of ensemble averages are required to produce reliable data. Another limitation of the DSMC models is the computational efficiency. For a typical micrometer scale simulation box, calculation takes at least several days to converge. In addition, it is difficult to accurately conserve energy and momentum at the phonon level in DSMC models. Considering these major limitations, in this work we use the variance reduced MC (VRMC) scheme developed by Professor Nicolas G. Hadjiconstantinou's group [79, 80, 89] at MIT. The VRMC models are described briefly in the following section, followed by some preliminary data on a silicon substrate covered with metallic nanodot heaters.

4.2 Variance Reduced MC Simulation

The details of the VRMC method can be found in reference [89] and are briefly reviewed here. The phonon BTE in its general form is shown in Eq. (3-1). Under the relaxation time approximation (RTA), the scattering term is simplified substantially and the BTE then becomes:

$$\frac{\partial f_\omega}{\partial t} + \overrightarrow{V_\omega} \cdot \nabla f_\omega = -\frac{f_\omega - f_{\omega 0}}{\tau_{\omega,T}} \qquad (4\text{-}1)$$

where f_ω is the spectral distribution function, $\overrightarrow{V_\omega}$ is the frequency dependent group velocity, $f_{\omega 0}$ is the locally thermalized distribution, and $\tau_{\omega,T}$ is the frequency and temperature dependent lifetime. Since all the derivatives in Eq. (4-1) are not with respect to phonon frequency, we can multiply that equation by the phonon energy $\hbar\omega$ and subtract a reference state to give:

$$\frac{\partial e^*}{\partial t} + \overrightarrow{V_\omega} \cdot \nabla e^* = -\frac{e^* - e_0^*}{\tau_{\omega,T}} \qquad (4\text{-}2)$$

where $e^* = \hbar\omega(f_\omega - f_\omega^{eq})$ is the deviational phonon energy distribution, and $e_0^* = \hbar\omega(f_{\omega 0} - f_{\omega 0}^{eq})$ is the locally thermalized deviational energy distribution. The reference distribution function f_ω^{eq} is the Bose-Einstein distribution evaluated at a reference temperature T_{eq}. Instead of solving the original BTE, VRMC models solve the deviational energy based BTE (i.e. Eq. (4-2)). By introducing a reference state, only the deviational part is stochastically simulated and the reference part can be exactly determined theoretically. This dramatically reduces the variance which occurs in DSMC simulations. By carefully choosing the reference state, VRMC simulation yields very clean signals even when temperature difference across the simulation domain is extremely small [80].

Due to the high SNR, the VRMC scheme enables us to simulate fewer particles and still yields reliable data, which consequently improves the computational efficiency. In addition to the enhanced efficiency, VRMC is advantageous over DSMC in terms of energy conservation. Phonons are simulated as energy particles, all of which represent some effective number of phonons and carry the same amount of energy. The uniform particle energy is determined by the total deviational energy divided by the particle number. For a simulation domain with E_{tot}^* (the total deviational energy) and N particles, each bundle carries the same amount of energy, $\varepsilon_{eff} = E_{tot}^*/N$, and represents some finite

number of real phonons, $N_{eff} = \varepsilon_{eff}/e^*$. This highlights the difference between DSMC and VRMC. Specifically, in DSMC the number of phonons per particle N_{eff} remains constant while for VRMC the effective energy per particle ε_{eff} is constant. Therefore, energy conservation in VRMC is quite easy and straightforward: conserving the number of particles automatically conserves the energy.

To carry out transport calculation, the simulation domain is discretized into a number of spatial cells. Each cell has its own local energy density and thus temperature. When the cell temperature T_0 is below the reference temperature T_{eq}, the deviational particle has negative energy since $e^* = \hbar\omega(f_\omega - f_\omega^{eq})$ is below zero. To account for this, we assign each particle a sign s(i) with it, where i is the particle index. Positive particles have positive signs s(i) = 1 while negative particles have negative signs s(i) = -1 [89]. The magnitude of the energy carried by each bundle is constant, but can be either positive or negative depending upon the local temperature relative to the reference temperature.

The following subsections discuss how to initialize the simulation, move particles, sample the local energy levels, and account for internal scattering.

4.2.1 Phonon Initialization

In VRMC models, phonons are initialized according to the initial temperature distribution across the simulation domain. Several approximations are needed to initialize the phonon particles. Due to the huge phonon number density and the computational limitation, we can simulate only a finite number of phonon particles. Effectively, one phonon bundle represents a bunch of physical phonons with the same transport properties, including the position $\vec{r}$, frequency ω, branch p, travelling velocity V_g, and propagation direction $\vec{k}$. These phonon properties must be initialized individually for all the particles to be simulated. The following paragraphs describe the details of how each phonon property is assigned.

- Position

Since the simulation domain is discretized, particles' initial positions are randomly assigned within each spatial cell. Specifically, for each drawn particle in cell (i, j, k), we generate three random numbers $R_x \in (0,1)$, $R_y \in (0,1)$, and $R_z \in (0,1)$ and assign the positions as:

$$x = x_c + (R_x - \tfrac{1}{2})\Delta x \qquad (4\text{-}3)$$

$$y = y_c + (R_y - \tfrac{1}{2})\Delta y \qquad (4\text{-}4)$$

$$z = z_c + (R_z - \tfrac{1}{2})\Delta z \qquad (4\text{-}5)$$

where (x_c, y_c, z_c) is the center of mass in the cell under study, and Δx, Δy, and Δz are the cell dimensions in x, y, z directions, respectively. All the generated particles in that cell are assigned positions in this way and this process is repeated for all the discretized cells. Therefore, phonon particles are populated randomly within the simulation domain.

- Frequency

After phonons are randomly placed in each spatial bin, the particles' frequencies are determined through a cumulative distribution function defined as:

$$F_n = \sum_{i=1}^{n} \sum_p D(\omega_i, \mathrm{p})e^* \qquad (4\text{-}6)$$

where $D(\omega, \mathrm{p})$ is the density of states (DOS) at a discretized angular frequency ω_i for a given polarization p. To initialize phonon frequencies, the material phonon dispersion is discretized uniformly into a set of frequency points N_b and the DOS for all the polarizations must be known. A random number R is drawn for each particle and compared with the cumulative distribution function F_n to generate the particle frequency. If R falls into the interval: $\frac{F_{n-1}}{F_{N_b}} < R < \frac{F_n}{F_{N_b}}$, the frequency is set to be:

$$\omega = \omega_n + (2R - 1)\frac{\Delta\omega}{2} \qquad (4\text{-}7)$$

where $\Delta\omega$ is the angular frequency interval. The random nature of R guarantees the randomness of ω assigned within that interval.

Note that temperature enters the cumulative function through the deviational energy e^*. In addition, if the local cell temperature T_0 is below the reference temperature T_{eq}, the cumulative distribution function carries negative sign. In this case, we use the normalized distribution function $|F_n|/|F_{N_b}|$ to initialize phonon frequencies and other procedures are kept the same. As discussed before, the generated particle has a negative sign when $T_0 < T_{eq}$.

- Polarization

To determine the branch information, another random number R_p is drawn for each particle and compared to DOS ratios. Here we only consider acoustic phonons to simplify the description, but optical phonons can be processed in the same manner. The selected phonon falls into longitudinal branch if $R_p < \frac{D(\omega,\text{LA})}{D(\omega,\text{TA1})+D(\omega,\text{TA2})+D(\omega,\text{LA})}$, where $TA1$, $TA2$, and LA denote two transverse acoustic branches and one longitudinal branch, respectively. Otherwise, a new random number R_{pp} is generated and again compared with another DOS ratio. The particle is assigned to $TA1$ branch if $R_{pp} < \frac{D(\omega,\text{TA1})}{D(\omega,\text{TA1})+D(\omega,\text{TA2})}$, otherwise it is assigned to $TA2$ branch. Typically particles are assigned to branches with higher DOS.

- Velocity and direction

Once frequency and branch are determined, the velocity is computed from the phonon dispersion relation $V_g = \frac{\partial\omega}{\partial k}$. The particle propagation angle is assigned randomly by generating two random numbers $R \in (-1,1)$ and $\phi \in (0,2\pi)$ as:

$$k_x = \sqrt{1 - R^2}\cos(\phi) \qquad (4\text{-}8)$$

$$k_y = \sqrt{1 - R^2}\sin(\phi) \qquad (4\text{-}9)$$

$$k_z = R \qquad (4\text{-}10)$$

After all the computational particles are assigned transport properties, they are allowed to move subject to the required boundary and interface conditions. Again, the total number of computational particles depends upon the deviational energy and the particle energy. Boundary and interface conditions are discussed in the following two subsections.

4.2.2 Advection & Boundary Scattering

In the advection step, only boundary and interface scattering are processed numerically. Within each time step, we follow the trajectory of all the particles and determine whether they collide with physical boundaries or interfaces. If the phonons collide with the physical walls, either the transport properties are reset or the phonons are removed from the domain, depending upon the boundary conditions (BCs). Methods for considering several different types of boundary conditions, including isothermal wall BC, periodic BC, and adiabatic wall BC, have been developed elsewhere [89] for use. Here we describe only two types of BCs in detail. Interested readers are referred to literature publications for the treatment of other BCs.

● Isothermal wall BC

In this case, consider a wall (for example at $x = 0$) at constant temperature T_w during the simulation. The wall is simulated as a phononic 'blackbody', which means that phonons colliding with the wall are absorbed and subsequently removed from the simulation domain. This boundary condition can be written as:

$$e_w^+[x = 0^+, k, p] = e_{T_w}^{eq}[x = 0^+, k, p] - e_{T_{eq}}^{eq}[\omega(k, p)] \qquad (4\text{-}11)$$

where $e_{T_w}^{eq}$ and $e_{T_{eq}}^{eq}$ are the deviational energy distributions evaluated at the wall temperature and the reference temperature, respectively. For the absorption, phonons incident on the isothermal wall are simply removed from the simulation domain. We can visualize the emission part by considering the wall as a heat reservoir, which constantly emits some number of phonons within each time step [89]. The number of phonon particles to be emitted is determined as follows:

$$N_w = \frac{1}{4}\sum_p \int_0^{\omega_{m,p}} D(\omega,p)V_g(\omega,p)e_w^* d\omega\Delta t \,/\varepsilon_{eff} \qquad (4\text{-}12)$$

where Δt is the time step. Computationally, phonons are emitted at the end of each advection step. The emission process is similar to the initialization step except that the cumulative distribution function is replaced by $F_n = \sum_{i=1}^{n}\sum_p D(\omega_i, p)V_g(\omega,p)e_w^*$. In addition, the travelling direction is assigned by generating two random numbers. $R_\theta \in (0,1)$ and $\phi \in (0,2\pi)$ and computing the direction as:

$$k_x = R_\theta \qquad (4\text{-}13)$$

$$k_y = \sqrt{1 - R_\theta^2}\sin(\phi) \qquad (4\text{-}14)$$

$$k_z = \sqrt{1 - R_\theta^2}\cos(\phi) \qquad (4\text{-}15)$$

- Periodic BC

Prediction of the properties of devices with periodic structures (for example, nanocomposites, comprised of two different periodically arranged materials) is critically important for practical applications. To simulate thermal transport in periodic structures, the use of periodic boundary condition significantly reduces the complexity and enhances the computational efficiency by simulating one period of the periodic structure. For

81

phonon transport in periodic systems, the heat flux is periodic, not the temperature, since the temperature gradient drives the heat flow. Here we derive the treatment of periodic boundary condition following reference [62].
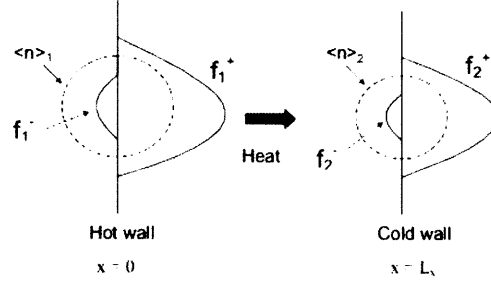
Figure 4-1 Diagram of periodic boundary condition [62].

Heat flux is generated by the deviation between the distribution function and an isotropic equilibrium distribution. As shown in Figure 4-1, the periodicity of heat flux can be expressed in terms of the distribution functions as:

$$f_1^+ - f_{T_1}^{eq} = f_2^+ - f_{T_2}^{eq} \qquad (4\text{-}16)$$

$$f_1^- - f_{T_1}^{eq} = f_2^- - f_{T_2}^{eq} \qquad (4\text{-}17)$$

where f_1^+, f_1^-, f_2^+, f_2^- are the forward and backward distribution functions at the periodic boundaries 1 and 2, respectively, and $f_{T_1}^{eq}$ and $f_{T_2}^{eq}$ are the isotropic equilibrium distributions associated with two different equilibrium boundary temperatures T_1 and T_2, respectively. Equations (4-16) and (4-17) show that the periodic heat flux is equivalent to the periodicity of the deviations in distribution functions. These expressions can also be written in terms of the deviational energy distribution as:

$$e_1^+ - e_{T_1}^{eq} = e_2^+ - e_{T_2}^{eq} \qquad (4\text{-}18)$$

$$e_1^- - e_{T_1}^{eq} = e_2^- - e_{T_2}^{eq} \tag{4-19}$$

We further rewrite Eqs. (4-18) and (4-19) in terms of the heat flux:

$$N_1^+ = N_2^+ + \tfrac{1}{4}\Sigma_p \int_0^{\omega_{m,p}} D(\omega, p)V_g(\omega, p)(e_{T_1}^{eq} - e_{T_2}^{eq})d\omega\Delta t /\varepsilon_{eff} \tag{4-20}$$

$$N_2^- = N_1^- + \tfrac{1}{4}\Sigma_p \int_0^{\omega_{m,p}} D(\omega, p)V_g(\omega, p)(e_{T_2}^{eq} - e_{T_1}^{eq})d\omega\Delta t /\varepsilon_{eff} \tag{4-21}$$

where N_1^+, N_2^+, N_1^-, N_2^- are the number of deviational particles that enter either the boundaries ('+') or the system ('−') of interest, respectively. Typically N_1^- and N_2^+ are known distributions from the simulation since they represent the phonons incident on either boundary (absorption part). The emission part, however, must be solved according to Eqs. (4-20) and (4-21). With VRMC, this can be done quite easily as follows:

i) In the advection step, particles traversing a periodic boundary are translated by one period in that direction to another corresponding periodic boundary where they are reinjected and continue moving until the end of the time step;

ii) At the end of each time step, we draw exactly $\tfrac{1}{4}\Sigma_p \int_0^{\omega_{m,p}} D(\omega,p)V_g(\omega,p)(e_{T_1}^{eq} - e_{T_2}^{eq})d\omega\Delta t /\varepsilon_{eff}$ deviational particles by pairs on both the hot and cold periodic boundaries and inject them into the simulation domain. Note that the injected particles from the hot wall carry positive signs while those emitted from the cold wall carry negative signs. In addition to the sign difference, the emitted phonon pairs from both boundaries have opposite travelling directions. In this way, we ensure the periodicity and conserve the energy in the simulation.

4.2.3 Internal Scattering

In addition to boundary and interface scattering, phonons also experience internal

scattering, including impurity and anharmonic scattering. The treatment of internal scattering follows reference [62]. In VRMC models, internal scattering is processed after each advection step. As discussed in reference [62], impurity scattering only randomizes the particle travelling direction and keeps other particle properties unchanged. However, anharmonic scattering resets all the phonon states and helps restore thermodynamic equilibrium. In general, anharmonic scattering includes the Normal process (N process) which conserves both energy and crystal momentum, and Umklapp process (U process) which only conserves energy [18, 20, 21].

The internal scattering event is treated as a probabilistic process in the VRMC models. Each scattering mechanism is described by a relaxation time, which depends upon phonon frequency and temperature and is an important input in the spectral VRMC calculations. Callaway [30] fit the thermal conductivity data of germanium at low temperatures to a phenomenological model for thermal conductivity including spectral phonon lifetimes in order to determine the strength of different scattering mechanisms which best reproduced the experimental data. A correction term to thermal conductivity was added in the model to account for the difference between the momentum-conserving N process and momentum-nonconserving U process. Unlike the treatment Callaway used for N process, Holland [31] treated N and U processes similarly, but differentiated the transverse and longitudinal branches to find the contributions from both polarizations. The combined phonon lifetime accounting for impurity scattering as well as both N and U processes is computed using Matthiessen's rule:

$$\tau_{\omega,T}^{-1} = \tau_N^{-1}(\omega, T) + \tau_U^{-1}(\omega, T) + \tau_I^{-1}(\omega) \tag{4-22}$$

where τ_N, τ_U, and τ_I are the relaxation time for N process, U process, and impurity scattering, respectively, at some frequency and temperature. To simplify the calculation, we combine the lifetime for N and U processes into a single lifetime τ_{NU}, where $\tau_{NU}^{-1} = \tau_N^{-1} + \tau_U^{-1}$, and do not differentiate those two scattering events.

To determine whether phonons experience internal scattering during each time step, we draw a random number R for each particle and compare it with $p(\omega) = 1 - \exp(-\frac{\Delta t}{\tau_{\omega,T}})$, where ω is the particle frequency, and Δt is the time step. Internal scattering occurs if R is less than $p(\omega)$. If internal scattering shows up, another random number R_{NU} is generated and compared with the scattering rate ratio $p_{NU}(\omega) = \frac{\tau_{NU}^{-1}(\omega)}{\tau_T^{-1}(\omega)}$. The deviational particle experiences anharmonic scattering if R_{NU} is less than $p_{NU}(\omega)$ and all the particle states are subsequently reset according to the corresponding cell temperature and pseudo-temperature. Otherwise, the particle is scattered by an impurity which only randomizes its propagation direction. The strategy to reset the phonons states as well as the concepts of cell temperature and pseudo-temperature are discussed in the following section.

4.2.4 Cell Temperature and Pseudo-temperature

To obtain the temperature distribution across the simulation domain, the phonon energy must be sampled in each spatial cell. Normally the energy is sampled immediately after the advection step. In the diffusive transport regime where the characteristic length scales are long compared to the phonon MFPs, a well-defined thermodynamic temperature exists under the assumption of local equilibrium. Nevertheless, in highly non-equilibrium or ballistic transport regime where scattering events are rare, the temperature cannot be defined since it is an equilibrium concept. In such case, the 'temperature' is known as the equivalent equilibrium temperature which is only a measure of the local energy density [18].

To calculate the temperature, we simply compute the energy density in each cell and invert it to obtain the corresponding cell temperature distribution. Energy sampling is made quite straightforward in VRMC since each deviational particle carries the same amount of energy. Thus we simply count the number of phonon particles within each cell

and add it to the reference energy density. The temperature is computed by comparing the local energy density to a pre-prepared Energy–Temperature table, which is calculated from the dispersion relation and DOS under different temperatures. The cell temperature distribution gives a sense of how 'hot' the region of interest is.

Another concept related to anharmonic phonon-phonon scattering is the pseudo-temperature, which is used to assist in resetting phonon states once anharmonic scattering occurs. Integrating Eq. (4-2) over all the phonon modes gives [62]:

$$\sum_p \int_0^{\omega_{max,p}} \left(\frac{\partial e^*}{\partial t} + \overrightarrow{V_\omega} \cdot \nabla e^*\right) D(\omega) d\omega = -\sum_p \int_0^{\omega_{max,p}} \frac{e^* - e_0^*}{\tau_{\omega,T}} D(\omega) d\omega \qquad (4\text{-}23)$$

where $\omega_{max,p}$ is the maximum phonon frequency for branch p, and T is the cell temperature. The first law of thermodynamics requires the left hand side of Eq. (4-23) to be exactly zero, which reduces Eq. (4-23) to become:

$$\sum_p \int_0^{\omega_{max,p}} \frac{e^*}{\tau_{\omega,T}} D(\omega) d\omega = \sum_p \int_0^{\omega_{max,p}} \frac{e_0^*}{\tau_{\omega,T}} D(\omega) d\omega \qquad (4\text{-}24)$$

The pseudo-temperature for the anharmonically scattered phonons is contained in the locally thermalized distribution function $e_0^* = \hbar\omega(f_{\omega 0} - f_{\omega 0}^{eq})$. Computationally, the local pseudo-temperature for each spatial cell is determined by inverting the local pseudo-energy density [89]:

$$\tilde{E}_{i,j,k} = \tilde{E}_{T_{eq}} + \frac{\varepsilon_{eff}}{V_{i,j,k}} \sum_q \frac{s(q)}{\tau_{\omega,p,T_{i,j,k}}} \qquad (4\text{-}25)$$

where $\tilde{E}_{T_{eq}} = \sum_p \int_0^{\omega_{m,p}} \frac{\hbar\omega D(\omega,p)}{\exp\left(\frac{\hbar\omega}{k_B T_{eq}}\right) - 1} \frac{1}{\tau_{\omega,p,T_{i,j,k}}} d\omega$ is the reference pseudo-energy at pseudo-temperature T_{eq}, (i, j, k) is the cell index, $T_{i,j,k}$ is the corresponding cell temperature, $V_{i,j,k}$ is the cell volume, q is the particle index, and $s(q)$ is the sign carried by each deviational particle. The summation in Eq. (4-25) is over all the particles

in cell (i, j, k). Similarly, the inversion process is done by comparing the local pseudo-energy to a pre-computed Pseudo-energy−Pseudo-temperature table.

If one computational particle experiences anharmonic scattering, all the phonon travelling states associated with that particle must be redrawn [62]. To reset the phonon properties and automatically satisfy the energy conservation, we use the new cumulative distribution function $\phi = \sum_p \frac{\hbar\omega D(\omega,p)}{\tau_{\omega,p,T_{i,j,k}}} (\frac{1}{\exp\left(\frac{\hbar\omega}{k_B \tilde{T}_{i,j,k}}\right)-1} - \frac{1}{\exp\left(\frac{\hbar\omega}{k_B T_{eq}}\right)-1})$, where $\tilde{T}_{i,j,k}$ is the pseudo-temperature in the cell (i, j, k), and $\tau_{\omega,p,T_{i,j,k}}$ is the phonon lifetime evaluated at the cell temperature $T_{i,j,k}$ [62].

4.2.5 Interface Conditions

Phonons incident on an interface are either reflected back or transmitted across the interface. Interface properties, including reflectivity and transmissivity, play an important role in determining heat flow across the interfaces. The reflectance and transmittance describe the probability of a phonon being reflected and transmitted at an interface, respectively. To evaluate interface transmissivities, we follow the transmission model presented in reference [75]. Energy must be conserved at the interface being studied. By simply linearizing the phonon distribution function and using the detailed balance [18, 75], the transmissivity $T_{12}(\omega)$ from side 1 to side 2 of an interface follows as:

$$\langle T_{12}(\omega)C_1 V_1 \rangle = \frac{2}{\frac{1}{\langle CV \rangle_1} + \frac{1}{\langle CV \rangle_2} + \frac{1}{2G}} \tag{4-26}$$

where C and V are the mode specific heat and group velocity, respectively, $\langle \cdot \rangle$ denotes an integral over the phonon modes, and G is the interface conductance. To simplify the analysis, we assume that $T_{12}(\omega)$ does not have any frequency dependence, and thus:

$$T_{12} = \frac{2/\langle C_1 V_1 \rangle^*}{\frac{1}{\langle CV \rangle_1} + \frac{1}{\langle CV \rangle_2} + \frac{1}{2G}}$$ (4-27)

where $\langle C_1 V_1 \rangle^*$ denotes integration over the shared phonon frequencies in materials 1 and 2. The transmissivity $T_{21}(\omega)$ from side 2 to side 1 follows directly from detailed balance:

$$T_{21}(\omega) = \frac{D_1(\omega) V_1(\omega)}{D_2(\omega) V_2(\omega)} T_{12}$$ (4-28)

where $D_i(\omega)$ and $V_i(\omega)$ (i=1, 2) are the mode dependent density of states and group velocity, respectively. Even if T_{12} is constant for common frequencies and zero otherwise, T_{21}, in general, bears a strong frequency dependence caused by the principle of detailed balance at each frequency. Note that mode conversion across the interface is suppressed to simply the transmission model.

4.2.6 Input Data and Assumptions

The required input data into the VRMC models include the phonon lifetimes, DOS, and dispersion relation for different phonon branches in addition to the interface transmissivities. For aluminum, heat is primarily carried by electrons. To simplify the calculations, we do not account for the electron phonon interaction in the metal film and only simulate the phonon transport. A constant relaxation time (10 ps) for all aluminum phonon modes is assumed and yields the desired phononic thermal conductivity 34 W/mK. Experimental dispersion relation for aluminum along [100] direction is used in this simulation [90].

For silicon, we input phonon lifetimes from empirical correlations to obtain some preliminary results [75, 81]. The silicon phonon lifetimes are listed below:

$$\tau_L^{-1} = 2 * 10^{-19} * \omega^2 T^{1.49} \exp(-\theta/T)$$ (4-29)

$$\tau_T^{-1} = 1.2 * 10^{-19} * \omega^2 T^{1.65} \exp(-\theta/T) \tag{4-30}$$

$$\tau_I^{-1} = 3 * 10^{-45} * \omega^4 \tag{4-31}$$

$$\tau_B^{-1} = 1.2 * 10^{-6} \tag{4-32}$$

where τ_L^{-1} and τ_T^{-1} are the anharmonic phonon scattering rates for longitudinal and transverse branches, respectively, and τ_I^{-1} and τ_B^{-1} are the impurity and boundary scattering rates, respectively. For the anharmonic scattering rates, an exponential term is used to extend the lifetimes to low temperatures [81]. For optical phonons, Einstein model which assumes a constant vibration frequency and zero travelling group velocity is used. Although optical phonons do not travel in a medium, they affect the transient thermal transport through the impact of heat capacity. The experimental dispersion relation along [100] crystal direction [91] is incorporated in the calculations.

4.3 Results and Discussion

The variance reduced Monte Carlo technique developed in the last section is applied to quantitatively study heat transport in the nanodot array spectroscopy experiments. Experimentally we lithographically deposit an array of square metallic dots of varying sizes onto the substrate of interest and observe heat transfer from the dots by illuminating the entire dot array with ultrafast lasers. The apparent substrate thermal conductivity is extracted by fitting the measured reflectance data with Fourier heat transfer model.

In this study, the Boltzmann transport equation in its most general form is solved with VRMC to compute the effective thermal conductivities for the three-dimensional complex structure shown in Fig. 2-3. The periodicity significantly simplifies the calculation by allowing us to simulate one period of the array. For the substrate, the four sides of the unit structure are assumed to be periodic boundaries. The top surface and four sides of the

metallic dot are approximated as diffuse adiabatic boundaries. Since the substrate is thick enough to be modeled as semi-infinite, the bottom surface of the substrate is considered to be isothermal with temperature fixed at the ambient level. In reality, as long as the substrate is sufficiently thick, we confirmed that the bottom boundary condition has little impact on the simulation results.

For the interface between the metallic dots and the silicon substrate, we use the model developed in section 4.2.6 to estimate the transmissivities across the interface. The interface conductance G is set to be approximately 1.1×10^8 W/m^{2}K, consistent with experimentally measured value. The interface transmission is crucially important in this simulation since it determines the heat flow rate from the heater to the substrate, and thus the cooling rate of the heater.

We start the simulation by launching several million deviational particles as an imposed temperature pulse in the heater. Those particles are allowed to move subject to the specified boundary conditions and also experience internal scattering. Gradually phonons in the heater traverse the interface into the substrate, thus cooling down the heater. The heater surface temperature is recorded as a function of the simulation time. Solutions from Fourier diffusive transport theory are fit to the VRMC results by varying the substrate thermal conductivity as a free fitting parameter in order to obtain the apparent thermal conductivity of the substrate as the heater size is systematically reduced.

The simulation is conducted for a silicon substrate with heaters at several different length scales. Figure 4-2 shows the calculated effective thermal conductivity data as a function of heater length scale. The silicon bulk thermal conductivity is approximately 145 W/mK at room temperature. For all the studied length scales, the effective thermal conductivities are below the bulk value. As discussed in previous chapters, this indicates that an additional ballistic resistance is observed [27, 32, 33] and the transport is quasi-ballistic. In addition, as the heater size is reduced, the calculated thermal conductivity drops steadily, which implies stronger size effects at shorter length scales.
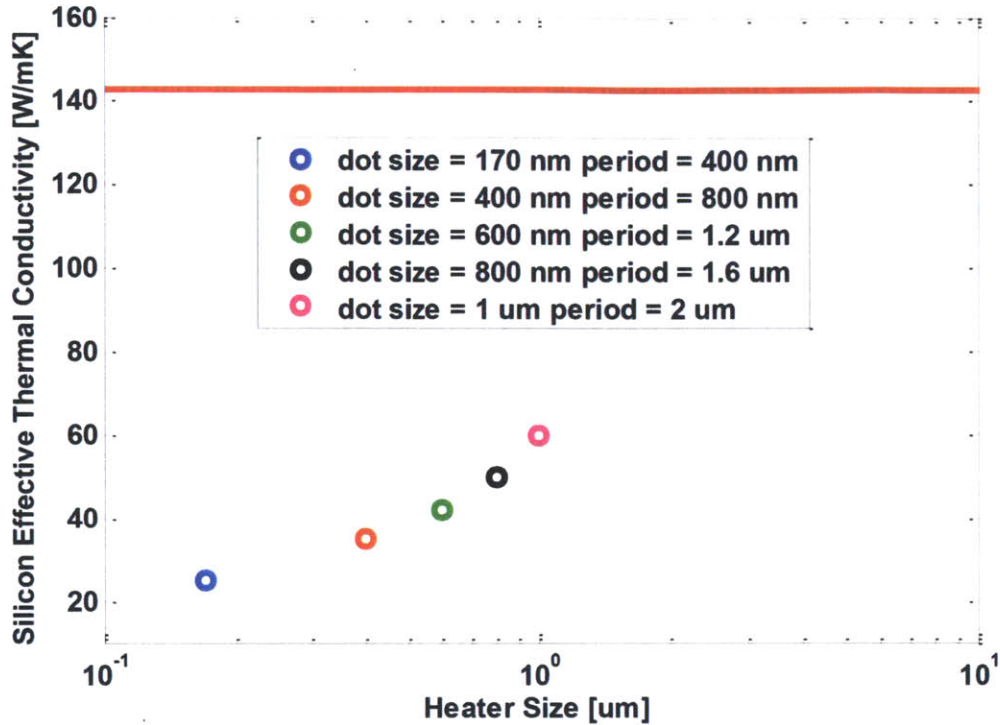
Figure 4-2 Calculated effective silicon thermal conductivity vs. heater length scales.

Physically, phonons with different MFPs in the heater transmit across the heater-substrate interface and experience scatterings depending on their MFPs relative to the heater dimension. We split the transmitted phonons into two groups [67]: a diffusive group ($\Lambda_\omega > D$) and a ballistic group ($\Lambda_\omega < D$), where Λ_ω and D are the spectral phonon MFP and heater size, respectively. The diffusive phonons scatter sufficiently and help restore thermodynamic equilibrium after transmission while the opposite is true for ballistic phonons [33]. Both components carry heat energy, but heat is dominantly transported via the diffusive phonons. Ballistic phonons rarely scatter around the interfacial region after transmission, thus they generate significantly less heat flux compared with the diffusive phonons [33]. The ballistic thermal resistance originates from ballistic phonons and increases with decreasing length scales, which is consistent with the lower calculated thermal conductivity at shorter length scales.

91

4.4 Summary

This chapter discusses a multidimensional spectrum dependent heat transfer model based upon a recently developed variance reduced Monte Carlo simulation technique. The model is applied to the study of quasi-ballistic transport in silicon by mimicking the spectroscopy experiments. Periodic and diffuse adiabatic boundary conditions are implemented to the boundaries of the simulation domain as required to model the spectroscopy experiments. Spectral interface properties are estimated from detailed balance by suppressing mode conversion at the interface. The calculated effective thermal conductivity shows a steady decrease with decreasing heater length scales, which is expected due to the increase in ballistic resistance at shorter characteristic length scales.

Chapter 5

Summary and Future Work

5.1 Summary

Nanotechnology offers a potential way to further enhance the thermoelectric figure of merit ZT by substantially reducing the material lattice thermal conductivity. Engineering better nanostructured thermoelectric materials demands better knowledge of the phonon mean free path (MFP) distribution in the materials of interest. In this thesis we have presented an experimental study of phonon MFPs in sapphire and two numerical studies to understand the quasi-ballistic phonon transport in the thermal conductivity spectroscopy experiments which are capable of determining the phonon MFPs down to nanoscale.

A thermal conductivity spectroscopy technique which has nanometer scale spatial resolution was combined with ultrafast TDTR experimental platform to study the phonon MFPs in sapphire, a non-absorbing material to the laser wavelength of our TDTR setup. By lithographically patterning nanometer scale metallic dot arrays on sapphire substrate, we probed the heat transfer down to 170 nm, far below the diffraction limit. The experimental observations of the quasi-ballistic phonon transport give information on the MFP distribution. The measured effective sapphire thermal conductivities at different heater length scales suggest phonon MFPs in sapphire are in the hundreds of nanometer

range, which is consistent with other measurements [27].

In the quasi-ballistic regime, heat transport is described by the general, spectral phonon Boltzmann transport equation (BTE) which determines the evolution of the phonon distribution function in phase space. In the first numerical study, a multidimensional thermal transport model based on the grey phonon BTE was developed. The diffuse mismatch model (DMM) was used to address the interface properties. Heat transfer in the structures of periodic nanowires on top of a generic substrate was studied using the developed grey transport model. Through simulations across a wide range of length scales, we found that two length scales (heater size and array period) significantly affected the apparent substrate thermal conductivity. Size effects were observed when the heater size was below half of the array period. In addition, the simulation data suggested different characteristic length scales in the quasi-ballistic transport have little impact on the thermal interface conductance.

In the second numerical study, we constructed another multidimensional frequency dependent heat transport model based on the recently developed variance reduced Monte Carlo (VRMC) method to account for the dispersive phonon spectrum. Variance reduced Monte Carlo method enables small signal detection in the simulations by introducing a reference state and solving only the deviational part. The interface transmissivities were estimated through a simple transmission model based on detailed balance. Quasi-ballistic phonon transport in the thermal conductivity spectroscopy experiments was studied using the constructed transport model. For each calculated heater length scale, solution of Fourier diffusive transport theory was fit to match the VRMC results by varying the substrate thermal conductivity. We observed the calculated effective silicon thermal conductivities dropped constantly with decreasing heater length scales. This suggested an increase in the ballistic thermal resistances as the heater length scale was reduced [27, 32, 33].

5.2 Future Research

Experimentally we plan to extend the developed thermal conductivity spectroscopy technique to probe the MFPs in thermoelectric materials. This is challenging since thermoelectric materials are in general non-transparent. A possible solution is to use hybrid nanostructures, which consists of periodically arranged light blocker dots and aluminum metallic dots sitting on substrate of interest. The light blocker dots have low absorptivity and low thermal conductivity. In this way the heated area is again effectively confined to the highly absorbing metallic dots. This allows phonon MFPs to be probed across wide ranges of length scales even for absorbing substrate materials. This structure has been recently developed by Dr. Yongjie Hu in Professor Chen's group.

In addition, accurate phonon MFP distribution cannot be quantified directly through the measurements of effective thermal conductivities at different heater length scales. To find the precise cumulative MFP distribution requires a heat flux suppression function [36, 37], which describes the heat flux generated by phonons with different MFPs relative to the prediction of diffusion theory. The suppression function can be found through Variance reduced Monte Carlo simulations across various length scales. The phonon MFPs can be reconstructed precisely from the spectroscopy measurement data and the suppression function.

Nanocomposites exhibit potential for high thermoelectric performance by introducing additional phonon scattering at interfaces. We also plan to apply the developed VRMC models to study the transport properties of complex nanocomposites. Molecular dynamics (MD) combined with Green-Kubo formula have been used to calculate lattice thermal conductivity under equilibrium conditions where no temperature gradient is imposed [92-94]. In such equilibrium transport, heat carriers move randomly with a zero averaged net heat flow rate. Motivated by equilibrium MD simulation, we will consider computing the thermal transport properties of materials of interest by applying the VRMC method at equilibrium state. This would also answer the question what information the heat carriers'

random motion contains.

Bibliography

[1] G. S. Nolas, J. Sharp, and H. J. Goldsmid. Thermoelectrics: Basic Principles and New Materials Developments. *Springer*, New York, 2001.

[2] C. Dames and G. Chen. Thermal conductivity of nanostructured thermoelectric materials. CRC Handbook, edited by M. Rowe, pp. 42-1 to 42-16, 2006, Taylor and Francis, Boca Raton.

[3] J. Yang. Potential applications of thermoelectric waste heat recovery in the automotive industry. In *24th International Conference on Thermoelectrics*, pp. 170–174, 2005.

[4] B. Poudel, Q. Hao,Y. Ma, Y. Lan, A. J. Minnich, B. Yu, X. Yan, D. Wang, A. Muto, D. Vashaee, X. Chen, J. Liu, M. S. Dresselhaus, G. Chen, and Z. F. Ren. High-thermoelectric performance of nanostructured bismuth antimony telluride bulk alloys. *Science*, 320(5876):634-638, 2008.

[5] A. I. Hochbaum, R. Chen, R. D. Delgado, W. Liang, E. C. Garnett, M. Najarian, A. Majumdar, and P. Yang. Enhanced thermoelectric performance of rough silicon nanowires. *Nature*, 451(7175):163-167, 2008.

[6] A. I. Boukai, Y. Bunimovich, J. Tahir-Kheli, J. Yu, W. A. Goddard III, and J. R. Heath. Silicon nanowires as efficient thermoelectric materials. *Nature*, 451(7175):168-171, 2008.

[7] R. Venkatasubramanian, E. Siivola, T. Colpitts, and B. O'Quinn. Thin film thermoelectric devices with high room-temperature figures of merit. *Nature*, 413(6856):597-602, 2001.

[8] S. Yamaguchi, T. Matsumoto, J. Yamazaki, N. Kaiwa, and A. Yamamoto. Thermoelectric properties and figure of merit of a Te-doped InSb bulk single crystal. *Applied Physics Letters*, 87(20):201902 - 3, 2005.

[9] J. K. Yu, S. Mitrovic, D. Tham, J. Varghese, and J. R. Heath. Reduction of thermal

conductivity in phononic nanomesh structures. *Nature Nanotechnology*, 5(10):718-721, 2010.

[10] G. Pernot, M. Stoffel, I. Savic, F. Pezzoli, P. Chen, G. Savelli, A. Jacquot, J. Schumann, U. Denker, I. Mönch, Ch. Deneke, O. G. Schmidt, J. M. Rampnoux, S. Wang, M. Plissonnier, A. Rastelli, S. Dilhaire, and N. Mingo. Precise control of thermal conductivity at the nanoscale through individual phonon-scattering barriers. *Nature Materials*, 9(6):491-495, 2010.

[11] M. S. Dresselhaus, G. Chen, Z. F. Ren, J.-P. Fleurial, P. Gogna, M.Y. Tang, D. Vashaee, H. Lee, X. Wang, G. Joshi, G. Zhu, D. Wang, R. Blair, S. Bux, and R. Kaner. Nanocomposites to enhance *ZT* in thermoelectrics. In *Proceedings of the MRS Fall Meeting*, page U3.4, Boston, 2007.

[12] A. J. Minnich, M. S. Dresselhaus, Z. F. Ren, and G. Chen. Bulk nanostructured thermoelectric materials: Current research and future prospects. *Energy and Environmental Science*, 2(5):466-479, 2009.

[13] A. J. Minnich, J. A. Johnson, A. J. Schmidt, K. Esfarjani, M. S. Dresselhaus, K. A. Nelson, and G. Chen. Thermal conductivity spectroscopy technique to measure phonon mean free paths. *Physical Review Letters*, 107(9):095901, 2011.

[14] M. Zebarjadi, K. Esfarjani, M. S. Dresselhaus, Z. F. Ren, and G. Chen. Perspectives on thermoelectrics: from fundamentals to device applications. *Energy and Environmental Science*, 5(1):5147-5162, 2012.

[15] W. J. Parker, R. J. Jenkins, C. P. Butler, and G. L. Abbott. Flash method of determining thermal conductivity, heat capacity, and thermal conductivity. *Journal of Applied Physics*, 32(9):1679, 1961.

[16] D. G. Cahill. Thermal conductivity measurement from 30K to 750K: the 3ω method. *Review of Scientific Instruments*, 61(2):802, 1990.

[17] C. A. Paddock and G. L. Eesley. Transient thermoreflectance from thin metal films. *Journal of Applied Physics*, 60(1):285, 1986.

[18] G. Chen. *Nanoscale Energy Transport and Conversion. Oxford University Press*, New York, 2005.

[19] G. A. Slack. CRC Handbook of Thermoelectrics, edited by DM Rowe (CRC Press, Boca Raton, FL, 1995).

[20] M. Lundstrom. *Fundamentals of Carrier Transport*. Cambridge University Press, 2000.

[21] N. W. Ashcroft and N. D. Mermin. *Solid State Physics*. Saunders college publishers, Fort Worth, TX, 1976.

[22] L. D. Hicks and M. S. Dresselhaus. Effect of quantum-well structures on the thermoelectric figure of merit. *Physical Review B*, 47(19):12727-12731, 1993.

[23] D. G. Cahill, W. K. Ford, K. E. Goodson, G. D. Mahan, A. Majumdar, H. J. Maris, R. Merlin, and S. R. Phillpot. Nanoscale thermal transport. *Journal of Applied Physics*, 93(2):793–818, 2003.

[24] G. Chen. Phonon transport in low-dimensional structures. In *Recent Trends in Thermoelectric Materials Research* III, volume 71 of Semiconductors and Semimetals, pages 203–259, 2001.

[25] G. Chen and A. Shakouri. Heat transfer in nanostructures for solid-state energy conversion. *Journal of Heat Transfer*, 124(2):242–252, 2002.

[26] Y. K. Koh and D. G. Cahill. Frequency dependence of the thermal conductivity of semiconductor alloys. *Physical Review B*, 76(7):075207, 2007.

[27] M. E. Siemens, Q. Li, R. Yang, K. A. Nelson, E. H. Anderson, M. M. Murnane, and H. C. Kapteyn. Quasi-ballistic thermal transport from nanoscale interfaces observed using ultrafast coherent soft X-ray beams. *Nature Materials*, 9(1):26-30, 2009.

[28] J. A. Johnson, A. A. Maznev, J. Cuffe, J. K. Eliason, A. J. Austin, T. Kehoe, C. M. Sotomayor Torres, G. Chen, and K. A. Nelson. Direct measurement of room-temperature nondiffusive thermal transport over micron distances in a silicon membrane. *Physical Review Letters*, 110(2):025901, 2013.

[29] K. Esfarjani, G. Chen, and H. T. Stokes. Heat transport in silicon from first-principles calculations. *Physical Review B*, 84(8):085204, 2011.

[30] J. Callaway. Model for lattice thermal conductivity at low temperatures. *Physical Review*, 113(4):1046, 1959.

[31] M. G. Holland. Analysis of lattice thermal conductivity. *Physical Review*, 132(6):2461, 1963.

[32] G. Chen. Nonlocal and nonequilibrium heat conduction in the vicinity of nanoparticles. *Journal of Heat Transfer*, 118(3):539-545, 1996.

[33] A. J. Minnich. *Exploring Electron and Phonon Transport at the Nanoscale for Thermoelectric Energy Conversion.* PhD Thesis, Massachusetts Institute of Technology, 2011.

[34] A. J. Schmidt, X. Chen, and G. Chen. Pulse accumulation, radial heat conduction, and anisotropic thermal conductivity in pump-probe transient thermoreflectance. *Review of Scientific Instruments*, 79(11):114902, 2008.

[35] J. A. Rogers, A. A. Maznev, M. J. Banet, and K. A. Nelson. Optical generation and characterization of acoustic waves in thin films: fundamentals and applications. *Annual Review of Materials Science*, 30(1):117-157, 2000.

[36] A. J. Minnich. Determining phonon mean free paths from observations of quasiballistic thermal transport. *Physical Review Letters*, 109(20):205901, 2012.

[37] A. A. Maznev, J. A. Johnson, and K. A. Nelson. Onset of non-diffusive phonon transport in transient thermal grating decay. *Physical Review B*, 84(19):195206, 2011.

[38] E. T. Swartz and R. O. Pohl. Thermal boundary resistance. *Review of Modern Physics*, 61(3):605–668, 1989.

[39] P. M. Norris and P. E. Hopkins. Examining interfacial diffuse phonon scattering through transient thermoreflectance measurements of thermal boundary conductance. *Journal of Heat Transfer*, 131(4):043207-043217, 2009.

[40] K.C. Collins, S. Chen, and G. Chen. Effects of surface chemistry on thermal conductance at aluminum-diamond interfaces. *Applied Physics Letters*, 97(8):083102, 2010.

[41] D. G. Cahill. Analysis of heat flow in layered structures for time-domain thermoreflectance. *Review of Scientific Instruments*, 75(12):5119, 2004.

[42] T. Q. Qiu and C. L. Tien. Short-pulse laser heating on metals. *International Journal of Heat and Mass Transfer*, 35(3):719–726, 1992.

[43] T. Q. Qiu and C. L. Tien. Heat transfer mechanisms during short-pulse laser heating of metals. *Journal of Heat Transfer*, 115(4):835 ‐ 841, 1993.

[44] T. Q. Qiu and C. L. Tien. Femtosecond laser heating of multi-layer metals - i. analysis. *International Journal of Heat and Mass Transfer*, 37(17):2789 - 2797, 1994.

[45] T. Q. Qiu, T. Juhasz, C. Suarez, W. E. Bron, and C. L. Tien. Femtosecond laser heating of multi-layer metals - ii. experiments. *International Journal of Heat and Mass Transfer*, 37(17):2799 - 2808, 1994.

[46] R. W. Schoenlein, W. Z. Lin, J. G. Fujimoto, and G. L. Eesley. Femtosecond studies of nonequilibrium electronic processes in metals. *Physical Review Letters*, 58(16):1680 - 1683, 1987.

[47] S. D. Brorson, J. G. Fujimoto, and E. P. Ippen. Femtosecond electronic heat transport dynamics in thin gold films. *Physical Review Letters*, 59(17):1962 - 1965, 1987.

[48] A. Majumdar and P. Reddy. Role of electron–phonon coupling in thermal conductance of metal–nonmetal interfaces. *Applied Physics Letters*, 84(23):4768, 2004.

[49] D. G. Cahill, K. Goodson, and A. Majumdar. Thermometry and thermal transport in micro/nanoscale solid-state devices and structures. *Journal of Heat Transfer*, 124(2):223 - 241, 2002.

[50] Y. Wang, J. Y. Park, Y. K. Koh, and D. G. Cahill. Thermoreflectance of metal transducers for time-domain thermoreflectance. *Journal of Applied Physics*, 108(4):043507, 2010.

[51] W. S. Capinski and H. J. Maris. Improved apparatus for picosecond pump-and-probe optical measurements. Review of Scientific Instruments, 67(8):2720, 1986.

[52] A. J. Schmidt. *Optical characterization of thermal transport from the nanoscale to the macroscale*. PhD thesis, Massachusetts Institute of Technology, 2008.

[53] K. C. Collins. *Experimental Investigations of Solid-Solid Thermal Interface Conductance*. Master thesis, Massachusetts Institute of Technology, 2010.

[54] M. N. Luckyanova. *Detecting Coherent Phonon Wave E_ects in Superlattices Using Time-Domain Thermoreectance*. Master thesis, Massachusetts Institute of Technology, 2012.

[55] Stanford Research Systems, "User's manual: Model SR844 RF lock-in amplifier",

2003.

[56] H. Carslaw and J. Jaeger. Conduction of Heat in Solids, pp. 64-70, 109-112. Oxford University Press, 1959.

[57] L. C. Andrews and B. K. Shivamoggi. *Integral Transforms for Engineers*. SPIE Optical Engineering Press, 1999.

[58] H.B.G. Casimir. Note on the conduction of heat in crystals. *Physica*, 5(6):495-500, 1938.

[59] W. J. de Haas and Th. Biermasz. The dependence on thickness of the thermal resistance of crystals at low temperatures. *Physica* 5(7), pp. 619-624, 1938.

[60] A. Majumdar. Microscale heat conduction in dielectric thin films. *Journal of Heat Transfer*, 115(1):7-16, 1993.

[61] S. V. J. Narumanchi, J. Y. Murthy, and C. H. Amon. Submicron heat transport model in silicon accounting for phonon dispersion and polarization. *Journal of Heat Transfer* 126(6):946-955, 2004.

[62] Q. Hao, G. Chen, and M.-S. Jeng. Frequency-dependent Monte Carlo simulations of phonon transport in two-dimensional porous silicon with aligned pores. *Journal of Applied Physics*, 106(11):114321, 2009.

[63] A. A. Joshi and A. Majumdar. Transient ballistic and diffusive phonon heat transport in thin films. *Journal of Applied Physics*, 74(1):31, 1993.

[64] G. Chen. Size and interface effects on thermal conductivity of superlattices and periodic thin-film structures. *Journal of Heat Transfer*, 119(2):220–229, 1997.

[65] G. Chen. Thermal conductivity and ballistic phonon transport in cross-plane direction of superlattices. *Physical Review B*, 57(23):14958–14973, 1998.

[66] G. Chen and T. Zeng. Nonequilibrium phonon and electron transport in heterostructures and superlattices. *Nanoscale and Microscale Thermophysical Engineering*, 5(2):71–88, 2001.

[67] G. Chen. Ballistic-diffusive heat conduction equations. *Physical Review Letters*, 86(11):2279-2300, 2001.

[68] G. Chen. Ballistic-diffusive equations for transient heat conduction from Nano- to Macroscales. *Journal of Heat Transfer*, 124(2):320-328, 2002.

[69] S. V. J. Narumanchi, J. Y. Murthy, and C. H. Amon. Simulation of unsteady small heat source effects in sub-micron heat conduction. *Journal of Heat Transfer*, 125(5):896-903, 2003.

[70] J. Y. Murthy and S. R. Mathur. An improved computational procedure for sub-micron heat conduction. *Journal of Heat Transfer*, 125(5):904-910, 2003.

[71] R. Yang and G. Chen. Thermal conductivity modeling of periodic two dimensional nanocomposites. *Physical Review B*, 69(19):195316, 2004.

[72] R. Yang, G. Chen, and M. S. Dresselhaus. Thermal conductivity of simple and tubular nanowire composites in longitudinal direction. *Physical Review B*, 72(12):125418, 2005.

[73] R. Yang, G. Chen, and M. S. Dresselhaus. Thermal conductivity modeling of core-shell and tubular nanowires. *Nano Letters*, 5(6):1111-1115, 2005.

[74] R. Yang, G. Chen, M. Laroche, and Y. Taur. Simulation of nanoscale multidimensional transient heat conduction problems using Ballistic-diffusive equations and phonon Boltzmann equation. *Journal of Heat Transfer*, 127(3):298-306, March 2005.

[75] A. J. Minnich, G. Chen, S. Mansoor, and B. S. Yilbas. Quasiballistic heat transfer studied using the frequency-dependent Boltzmann transport equation. *Physical Review B*, 84(23):235207, 2011.

[76] J. M. Ziman. *Electrons and Phonons*. Clarendon Press, Oxford, 1960.

[77] P. Reddy, K. Castelino, and A. Majumdar. Diffuse mismatch model of thermal boundary conductance using exact phonon dispersion. *Applied Physics Letters*, 87(21):211908, 2005.

[78] L. J. Challis. Kapitza resistance and acoustic transmission across boundaries at high frequencies. *Journal of Physic C*, 7(3):481-495, 1974.

[79] N. G. Hadjiconstantinou, G. A. Radtke, and L. L. Baker. On variance-reduced simulations of the Boltzmann transport equation for small-scale heat transfer applications. *Journal of Heat Transfer*, 132(11):112401-112408, 2010.

[80] J. M. Peraud and N.G. Hadjiconstantinou. Efficient simulation of multi-dimensional phonon transport using energy-based variance-reduced Monte Carlo formulations. *Physical Review B*, 84(20):205331, 2011.

[81] A. S. Henry and G. Chen. Spectral phonon transport properties of silicon based on molecular dynamics simulations and lattice dynamics. *Journal of Computational and Theoretical Nanoscience*, 5(2):141-152, 2008.

[82] A. Ward and D. A. Broido. Intrinsic phonon relaxation times from first principles studies of the thermal conductivities of Si and Ge. *Physical Review B*, 81(8):085205, 2010.

[83] T. Klitsner, J. E. VanCleve, H. E. Fischer, and R. O. Pohl. Phonon radiative heat transfer and surface scattering. *Physical Review B*, 38(11):7576–7594 (1988).

[84] R. B. Peterson. Direct simulation of phonon-mediated heat transfer in a Debye crystal. *Journal of Heat Transfer*, 116(4):815-822, 1994.

[85] S. Mazumder and A. Majumdar. Monte Carlo study of phonon transport in solid thin films including dispersion and polarization. *Journal of Heat Transfer*, 123(4):749-759, 2001.

[86] Y. Chen, D. Li, J. R. Lukes, and A. Majumdar. Monte Carlo simulation of silicon nanowire thermal conductivity. *Journal of Heat Transfer*, 127(10):1129-1137, 2005.

[87] W. Tian and R. Yang. Thermal conductivity modeling of compacted nanowire composites. *Journal of Applied Physics*, 101(1): 054320, 2007.

[88] M.-S. Jeng, R. Yang, D. Song, and G. Chen. Modeling the thermal conductivity and phonon transport in nanoparticle composites using Monte Carlo simulation. *Journal of Heat Transfer*, 130(4):042410-11, 2008.

[89] J. M. Peraud. *Low Variance Methods for Monte Carlo Simulation of Phonon Transport*. Master thesis, Massachusetts Institute of Technology, 2011.

[90] R. Stedman and G. Nilsson. Dispersion relations for phonons in aluminum at 80 and 300°K. *Physical Review B*, 145(2):492-500, 1966.

[91] B. N. Brockhouse. Lattice vibrations in silicon and germanium. *Physical Review Letters*, 2(6):256-258, 1959.

[92] M. S. Green. Markoff random processes and the statistical mechanics of time-dependent phenomena. II. Irreversible processes in fluids. *Journal of Chemical Physics*, 22(3):398-413, 1954.

[93] R. Kubo. Statistical-mechanical theory of irreversible processes. I. General theory and simple applications to magnetic and conduction problems. *Journal of the Physical Society of Japan*, 12(6):570-586, 1957.

[94] S. G. Volz and G. Chen. Molecular-dynamics simulation of thermal conductivity of silicon crystals. *Physical Review B*, 61(4):2651-2656, 2000.